Ice crystal number concentration estimates from lidar-radar satellite remote sensing. Part 1: Method and evaluation

Odran Sourdeval[1], Edward Gryspeerdt[2], Martina Krämer[3], Tom Goren[1], Julien Delanoë[4],
Armin Afchine[3], Friederike Hemmer[5], and Johannes Quaas[1]

[1]Institute for Meteorology, Universität Leipzig, Leipzig, Germany
[2]Space and Atmospheric Physics Group, Imperial College London, London, UK
[3]Forschungszentrum Jülich, Institut für Energie und Klimaforschung (IEK-7), Jülich, Germany
[4]LATMOS/UVSQ/IPSL/CNRS, Guyancourt, France
[5]Laboratoire d'Optique Atmosphérique, Université Lille1, Villeneuve d'Ascq, France

Correspondence: Odran Sourdeval (odran.sourdeval@uni-leipzig.de)

Abstract. The number concentration of cloud particles is a key quantity for understanding aerosol-cloud interactions and describing clouds in climate and numerical weather prediction models. In contrast with recent advances for liquid clouds, few observational constraints exist on the ice crystal number concentration (N_i). This study investigates how combined lidar-radar measurements can be used to provide satellite estimates of N_i, using a methodology that constrains moments of a parameterized particle size distribution (PSD). The operational liDAR-raDAR (DARDAR) product serves as an existing base for this method, which focuses on ice clouds with temperatures $T_c < -30°C$.

Theoretical considerations demonstrate the capability for accurate retrievals of N_i, apart from a possible bias in the concentration in small crystals when $T_c \gtrsim -50°C$, due to the assumption of a monomodal PSD shape in the current method. This is verified by comparing satellite estimates to co-incident in situ measurements, which additionally demonstrates the sufficient sensitivity of lidar-radar observations to N_i. Following these results, satellite estimates of N_i are evaluated in the context of a case study and a preliminary climatological analysis based on 10 years of global data. Despite of a lack of other large-scale references, this evaluation shows a reasonable physical consistency in N_i spatial distribution patterns. Notably, increases in N_i are found towards cold temperatures and, more significantly, in the presence of strong updraughts, such as those related to convective or orographic uplifts. Further evaluation and improvements of this method are necessary but these results already constitute a first encouraging step towards large-scale observational constraints for N_i. Part two of this series uses this new dataset to examine the controls on N_i.

1 Introduction

Clouds play a major role in the climate system and are essential components of the Earth-atmosphere radiation balance (Stephens, 2005). A precise understanding of their properties and processes therefore is necessary to properly address current uncertainties of climate change estimates (Boucher et al., 2013). In particular, the impact of ice clouds on the Earth's radiation budget is recognized as being substantial (e.g. Liou, 1986; Stephens et al., 1990) but still remains difficult to quantify

due to the large variability and complexity of their radiative, macro- and micro-physical properties (Zhang et al., 1999; Baran, 2009).

Because of their high spatial and temporal coverage, satellite observations are excellent tools to answer these questions (Lohmann et al., 2007). The A-Train satellite constellation offers a unique synergy between a wide range of active and passive

5 instruments (Stephens et al., 2002), such that numerous methods now exist to provide spaceborne retrievals of ice cloud properties. For instance, bi-spectral approaches based passive visible (Nakajima and King, 1990) or thermal infrared (Inoue, 1985) measurements are often used to directly infer the cloud optical depth (τ_c) and ice crystal effective radius (r_{eff}) (e.g. King et al., 1998; Sourdeval et al., 2013). Direct retrievals of the vertically integrated ice water content (IWC) - the ice water path (IWP) - can also be obtained from these channels (Sourdeval et al., 2015), passive microwave sensors (Gong and Wu, 2014),

10 or a synergy of both (Holl et al., 2014). Vertical profiles of the cloud visible extinction (α_{ext}), IWC and ice crystal r_{eff} are commonly provided using lidar and/or radar measurements (e.g. Vaughan et al., 2009; Austin et al., 2009; Delanoë and Hogan, 2010). However, only few developments have to date focused on the ice crystal number concentration (N_i).

A lack of N_i retrievals from satellite contrasts with the importance of this quantity for understanding and describing ice cloud processes (Comstock et al., 2008). Along with the mass concentration, the number concentration is often used as a

15 prognostic variable in two-moment bulk microphysics schemes that predict the evolution of clouds in recent climate and numerical weather prediction models (Khain et al., 2000; Seifert and Beheng, 2006). An absence of global observational constraints therefore limits the evaluation of model predictions to sparser in situ measurements (e.g. Jensen et al., 1994; Zhang et al., 2013; Farrington et al., 2016). Moreover, N_i appears as a particularly useful metric to quantify aerosol-cloud interactions due its potentially close link with the aerosol concentration (Kärcher and Ström, 2003; Kay and Wood, 2008; Hendricks et al.,

20 2011). Consequently, while numerous studies have for these reasons used satellite estimates of the cloud droplet number concentration (N_d) to evaluate the indirect aerosol radiative forcing (Boers et al., 2006; Quaas et al., 2006, 2008; Gryspeerdt et al., 2016), the contribution of ice clouds to this effect remains largely unknown (Heyn et al., 2017).

One reason for this absence of a global N_i dataset lies in the difficulty to directly link this quantity to other commonly retrieved cloud properties. For liquid clouds, N_d can for instance be inferred through relationships between satellite retrievals

25 of τ_c and the droplet r_{eff} (Brenguier et al., 2000). These relationships rely on strong assumptions that have shortcomings (Grosvenor et al., 2018) but nonetheless provide N_d values that compare well against in situ observations (Painemal and Zuidema, 2011) and can be used to establish climatologies (Bennartz and Rausch, 2017). Such relationships are less trivial for ice clouds due to the high complexity and variability of ice nucleation processes (Kärcher and Lohmann, 2002, 2003; Ickes et al., 2015). Recent attempts have been made, e.g. by Mitchell et al. (2016) who linked (providing additional lidar information)

30 the absorption τ_c and ice crystal r_{eff} to N_i for thin single-layer ice clouds, but rigorous validation remains necessary.

An alternative approach to estimate N_i has arisen with the emergence of retrieval methods aiming at directly constraining parameters of particle size distributions (PSDs) from remote sensing observations. Indeed, provided that a PSD is properly estimated, the corresponding number concentration (the zeroth moment of the PSD, or $\mathcal{M}_0$) can be extracted. Important developments on applying these methods to satellite observations can be attributed to Austin and Stephens (2001) who, through

35 an elaborate variational scheme, used the sensitivity of radar reflectivity (Z_e) and τ_c to other moments, namely $\mathcal{M}_6$ and $\mathcal{M}_2$,

respectively, to constrain PSD shape parameters. This method, initially dedicated to liquid clouds, allowed retrieving profiles of droplet geometric mean radius and a vertically homogeneous N_d. This work was later extended to ice clouds by Benedetti et al. (2003) and further improved by Austin et al. (2009) to perform retrievals of N_i profiles using better *a priori* assumptions. These developments are now implemented in the operational CloudSat 2B-CWC-RO product, which has extensively been used

5 to study the IWC (e.g. Wu et al., 2009; Waliser et al., 2009; Eliasson et al., 2011) but its N_i product remains to be thoroughly evaluated. Notably, Protat et al. (2010) highlighted through comparisons to ground-based lidar-radar cloud products the need to improve these N_i retrievals prior to quantitative use. The authors argued that radar-only methods lack sensitivity to N_i profiles due to the dominant contribution of small ice particles to the total number concentration, whereas the combined use of a lidar extinction backscatter coefficient (β_{ext}) would help to further constrain the amount of small particles. However, no operational

10 estimation of N_i from satellite lidar-radar observations has to date been attempted.

Based on these early developments, this study aims at investigating the capabilities of lidar-radar methods to estimate N_i by producing and evaluating a new dataset based on the operational liDAR-raDAR (DARDAR, Delanoë and Hogan, 2010) product. DARDAR retrieves profiles of ice cloud properties by combining measurements from the CloudSat Cloud Profiling Radar (CPR) and the Cloud-Aerosol Lidar with Orthogonal Polarization (CALIOP). Although DARDAR does not operationally

15 provide N_i, and has not been tested for this purpose, its retrieval framework that aims at constraining parameters of a PSD parameterization (Delanoë et al., 2005, hereinafter D05) makes it an suitable candidate to estimate this quantity. Nevertheless, a careful evaluation remains necessary to determine if the D05 parameterization is theoretically capable of predicting N_i and if lidar-radar measurements can provide sufficient information to properly constrain it. Therefore, a threefold evaluation is performed here to investigate the quality of these lidar-radar N_i estimates based on comparisons to in situ observations, a case

20 study and a brief climatological analysis.

The paper is structured as follow: Section 2 presents the methodology used here to estimate N_i from current DARDAR products. Sec. 3 describes the data utilized in this study. The ability of DARDAR to retrieve in situ measurements of N_i is investigated in Sec. 4. Then, Sec. 5 discusses the vertical structure of N_i estimates along a short orbit and Sec. 6 proposes a brief analysis of N_i climatologies. Finally, Sec. 7 concludes this study. The second part of this series (?) will use this new

25 dataset to investigate the processes controlling N_i.

2 Methodology

2.1 The DARDAR product

For brevity reasons, this section only provides an introduction to the DARDAR product; the reader is invited to refer to Delanoë and Hogan (2008, 2010) for a thorough description of the retrieval method.

30 DARDAR (currently v2.1.1) uses a variational framework to merge information from β_{ext} and Z_e profiles in order to retrieve vertical structures of ice cloud α_{ext} and of a parameter noted N_0^*. These two parameters, which are closely linked to a PSD parameterization (see Sec. 2.2), are subsequently combined to infer profiles of IWC and ice crystal r_{eff}. The lidar and radar measurements are provided by CALIOP and CPR, respectively, which implies that DARDAR retrieves cloud properties with

a vertical resolution of $60\,\mathrm{m}$ along the CloudSat footprint (about $1.7\,\mathrm{km}$ of horizontal resolution). It is worth noting that the simultaneous use of lidar and radar information allows this method to be sensitive to thick and thin ice clouds, with IWPs spanning from about $0.01\,\mathrm{g.m^{-2}}$ to $5\,\mathrm{kg.m^{-2}}$ (Sourdeval et al., 2016). The position and thermodynamic phase of cloud layers (DARDAR mask, v1.1.4; e.g. Ceccaldi et al., 2013) are determined, prior to the retrieval process, using these measurements
5 and reanalyses from the European Centre for Medium-Range Weather Forecasts (ECMWF).

DARDAR has already been extensively used for improving our understanding of clouds and precipitation (e.g. Battaglia and Delanoë, 2013; Protat et al., 2014; Feofilov et al., 2015; Massie et al., 2016). Its operational retrievals have also been evaluated against products from a similar lidar-radar method (CloudSat 2C-ICE; Deng et al., 2010) and in situ observations. Deng et al. (2012) found good agreements between the retrievals of the IWC, r_{eff} and α_v from both methods, which also compared well
10 against co-incident in situ observations, despite a small overestimation noted for IWCs retrieved by DARDAR in lidar-only conditions.

2.2 Representation of the size distribution

N_i can be expressed as the integral of a given ice particle size distribution $N(D)$,

$$N_i = \mathcal{M}_0 = \int_0^\infty N(D)dD, \tag{1}$$

15 with D the particle dimension (hereinafter the maximum diameter). Hence, N_i corresponds to the moment zero of the PSD, noted $\mathcal{M}_0$. Other moments also relate to various cloud properties (e.g. to the IWC, through mass-dimension relations, or to $D_{\mathrm{eff}} = \mathcal{M}_3/\mathcal{M}_2$) and to remote sensing measurements (e.g. β_{ext} relates to $\mathcal{M}_2$ and Z_e to $\mathcal{M}_6$), demonstrating that PSDs act as crucial links between physical parameters and observations. However, although β_{ext} and Z_e are sensitive to particle sizes, they each provide information on a single moment of the PSD. Therefore, assuming a pair of single-wavelength measurements, their
20 combination is not sufficient to fully constrain every aspect of a complex PSD; simplifications are necessary. Parameterizing PSDs is a challenging task due to the large variability of their shapes on a global scale or even within a cloud layer (e.g. Mitchell et al., 2011; Krämer et al., 2016). Nevertheless, D05 and Field et al. (2005) showed that two-moment normalization methods can be used to reasonably approximate a wide range of measured size distributions to a single shape function, noted F, referred to as a "universal" or "normalized" PSD. By normalization it is meant that the dimension and concentration axes
25 are carefully scaled in order to make F independent of parameters that strongly influence the shape of the original PSD.

In the framework by D05, which is implemented in DARDAR, a normalization factor noted N_0^* and the ice crystal mean volume-weighted diameter D_{m} (defined as the ratio of $\mathcal{M}_4$ to $\mathcal{M}_3$) serve as scaling parameters to the concentration and dimension axes, respectively. The normalization process can thus be summarized as

$$F(D_{\mathrm{eq}}/D_{\mathrm{m}}) = N(D_{\mathrm{eq}})/N_0^*, \tag{2}$$

30 where D_{m} and N_0^* are in D05 specifically set to make F independent of the IWC and D_{m} of the original PSD (i.e. they become constant after normalization). The ice crystal size is represented by the equivalent-melted diameter, D_{eq}, which relates to D

through

$$D_{\text{eq}} = \left[\frac{6m(D)}{\pi \rho_w} \right]^{\frac{1}{3}}, \tag{3}$$

where $\rho_w = 1000 \, \text{kg} \, \text{m}^{-3}$ is the density of liquid water and $m(D)$ is a given mass-dimension (m-D) relationship. In DARDAR, the latter follows empirical formulas by Brown and Francis (1995) when $D > 300 \, \mu\text{m}$ and by Mitchell (1996) otherwise. D05 demonstrated with in situ measurements that this approach allows the accurate prediction of $\mathcal{M}_2$ and $\mathcal{M}_6$. Inversely, β_{ext} and Z_e can be used to constrain these moments, infer the associated scaling parameters and reproduce the original PSD using Eq. (2). Regarding the shape of $N(D_{\text{eq}})$, D05 concluded that a four-parameter gamma-modified distribution,

$$N(D_{\text{eq}}) = N_0 D_{\text{eq}}^{\alpha} \exp\{-k D_{\text{eq}}^{\beta}\}, \tag{4}$$

allows the parameterization to properly fit in situ measurements from mid-latitude and tropical regions. α and β are two fixed parameters that were adjusted to best fit these measurements ($\alpha = -1$ and $\beta = 3$). On the contrary, N_0 and k vary during the retrieval process, where they are iteratively adjusted to fit observational constraints through their relations to the scaling parameters, as shown in Sec. 2.3.

2.3 Extracting N_i from DARDAR

Considering the gamma-modified function of Eq. (4) to describe the shape of $N(D)$ in Eq. (1), and because the total number of particles is independent of the choice of a dimensional variable, N_i in DARDAR corresponds to

$$N_\text{i} = \int_0^{+\infty} N_0 D_{\text{eq}}^{\alpha} \exp\{-k D_{\text{eq}}^{\beta}\} dD_{\text{eq}}. \tag{5}$$

Because α and β are fixed, N_i can be obtained given a knowledge of N_0 and k. These two parameters are not part of the operational products but can be deduced from their link to other retrieved properties. This section shows how N_i can be inferred from IWC and N_0^*, which are both operationally provided. It should be kept in mind that a strict consistency with the current version of the algorithm must be respected to ensure that N_i estimates are meaningful; possible improvements, such as proposed by Delanoë et al. (2014) for future DARDAR versions, are not included at this stage.

As mentioned in Sec. 2.2, the scaling parameters N_0^* and D_m are defined so that $N(D_{\text{eq}})$ becomes independent of IWC and D_m after normalization. Using the definition of $N(D_{\text{eq}})$ from Eq. (2) to rewrite $D_\text{m} = \mathcal{M}_4 / \mathcal{M}_3$, the latter condition leads to $\mathcal{M}_4^F = \mathcal{M}_3^F$, with $\mathcal{M}_n^F$ the nth moment of the normalized PSD $F(D_{\text{eq}}/D_\text{m})$. Subsequently, $\mathcal{M}_3^F$ and $\mathcal{M}_4^F$ must be equal to an arbitrary constant, which was set by D05 to $\Gamma(4)/4^4$. By inserting Eq. (4) into Eq. (2), and after simplification of the definite integral, $\mathcal{M}_n^F$ becomes

$$\mathcal{M}_n^F = \frac{1}{\beta} \Gamma\left(\frac{\alpha + n + 1}{\beta} \right) \frac{N_0}{N_0^*} D_\text{m}^{-(n+1)} k^{-\frac{\alpha+n+1}{\beta}}. \tag{6}$$

Based on this equation, the conditions $\mathcal{M}_4^F = \mathcal{M}_3^F$ and $\mathcal{M}_3^F = \Gamma(4)/4^4$ lead to two unique relationships between the PSD parameters k and N_0 and the scaling parameters:

$$k = \left[\frac{1}{D_\mathrm{m}} \frac{\Gamma\left(\frac{\alpha+5}{\beta}\right)}{\Gamma\left(\frac{\alpha+4}{\beta}\right)} \right]^\beta \qquad (7)$$

and

$$N_0 = \mathrm{N}_0^* D_\mathrm{m}^{-\alpha} \frac{\Gamma(4)}{4^4} \beta \frac{\Gamma\left(\frac{\alpha+5}{\beta}\right)^{\alpha+4}}{\Gamma\left(\frac{\alpha+4}{\beta}\right)^{\alpha+5}}, \qquad (8)$$

respectively. Hence, providing N_0^* and D_m, Eq. (7) and (8) can be inserted into Eq. (5) to compute $\mathrm{N_i}$. The scaling parameter N_0^* is provided in DARDAR, whereas D_m can be deduced from other cloud properties. The IWC, which by definition equals $\frac{\pi\rho_w}{6}\mathcal{M}_3$ for equivalent-melted spheres, can be related to N_0^* and D_m. By using Eq. (2) to demonstrated that $\mathcal{M}_3 = \mathrm{N}_0^* D_\mathrm{m}^4 \mathcal{M}_3^F$ and, because $\mathcal{M}_3^F = \Gamma(4)/4^4$, D_m can be inferred from IWC and N_0^* following

$$D_\mathrm{m} = 4 \left[\frac{1}{\pi\rho_w} \frac{\mathrm{IWC}}{\mathrm{N}_0^*} \right]^{\frac{1}{4}}. \qquad (9)$$

3 Data description

3.1 Satellite retrievals

DARDAR IWC and N_0^* retrievals from 2006 to 2016 are used here to compute a 10-year $\mathrm{N_i}$ dataset based on the methodology described in Sec. 2. It can be noted that the DARDAR products are not continuously available throughout this period due to gaps in the CloudSat measurements but such discontinuities should not affect the following conclusions as precise analyses of $\mathrm{N_i}$ patterns (e.g. trends or diurnal cycles) are not intended in this study. To avoid possible confusion with the operational product, the research-level $\mathrm{N_i}$ dataset obtained here will be referred to as DARDAR-LIM (DARDAR - Leipzig Institute for Meteorology).

In order to limit erroneous retrievals, two filters were applied to DARDAR-LIM. First, $\mathrm{N_i}$ is only computed for purely ice clouds that are not situated below supercooled or liquid layers (i.e. layers identified as supercooled or mixed-phase by the DARDAR mask are ignored). This condition is required to avoid possibly strong uncertainties in retrievals of the cloud phase and/or properties. Then, pixels where DARDAR converged too quickly, i.e. with a number of iterations $\mathrm{n_{iter}} \leqslant 2$, are ignored in order to limit any strong influence of *a priori* assumptions on the retrieved cloud properties.

It should be mentioned that DARDAR provides uncertainties associated with its retrievals, obtained by the propagation of errors related to the measurements and non-retrieved forward model parameters. However, no transcriptions into errors on $\mathrm{N_i}$ are shown in this study as they are unlikely to be meaningful for this quantity. Indeed, no uncertainty is associated with the PSD shape, whose representation of the small ice crystal distribution is crucial to $\mathrm{N_i}$. Instead, an estimation of the quality of the DARDAR-LIM dataset will be reached through comparisons to in situ measurements.

3.2 In situ measurements

In situ PSD measurements from mid-latitude and tropical ice clouds are required to evaluate the satellite estimates of N_i. This evaluation must determine if (i) the PSD parameterization used in DARDAR (i.e. D05) is capable of predicting $\mathcal{M}_0$, and (ii) there is enough sensitivity in lidar-radar measurements to properly constrain N_i. A few conditions are thus set for this

5 evaluation. To answer (i), it is preferable that the measurements used in this evaluation are independent of the ones utilized by D05 to build the PSD parameterization. Answering (ii) additionally requires measurements from flights that are coincident with the CloudSat overpass. Finally, (i) and (ii) require usable measurements of the concentration in small ice crystals (i.e. $D < 100 \, \mu$m), which highly contribute to N_i. This implies that possible phenomena of ice crystal shattering on the probe tips and inlets (Korolev et al., 2011, 2013) must be accounted for to a reasonable extent, through combined specific instrumental

10 design and post-processing (Field et al., 2006; Korolev and Field, 2015).

3.2.1 Airborne instruments and campaigns

Table 1. Description of the in situ campaigns. The numbers correspond to PSDs averaged into 10-s periods and for ice clouds with $T_c < -30°$C.

Campaign	Instrument(s)	$\overline{\text{TAS}}$	#PSDs / Eq. sampling time
COALESC 2011	NIXE-CAPS	168 m.s^{-1}	3459 / 9.6 h
ML-CIRRUS 2014	NIXE-CAPS	207 m.s^{-1}	5954 / 16.5 h
ACRIDICON-CHUVA 2014	NIXE-CAPS	209 m.s^{-1}	4166 / 11.6 h
SPARTICUS 2010	2D-S	174 m.s^{-1}	15090 / 41.9 h
ATTREX 2014	FCDP / 2D-S	157 m.s^{-1}	11465 / 31.8 h

Measurements from five recent airborne campaigns are used during this evaluation process. Three campaigns are described in the 'Cirrus Guide Part I' by Krämer et al. (2016), namely COALESC 2011 (Combined Observation of the Atmospheric boundary Layer to study the Evolution of Strato-Cumulus; Osborne et al., 2014), ML-CIRRUS 2014 (Mid-Latitude CIRRUS; Voigt

15 et al., 2016) ACRIDICON-CHUVA 2014 (Aerosol, Cloud, Precipitation, and Radiation Interactions and Dynamics of Convective Cloud Systems; Wendisch et al., 2016). Another two campaigns took place over the US and tropical Pacific: SPARTICUS 2010 (Small PARticle In CirrUS; Mace et al., 2009) and ATTREX 2014 (Airborne Tropical TRopopause EXperiment-2014; Jensen et al., 2015). A detailed description of these field campaigns and of their involved instrumentation can be found in the above-mentioned references and is therefore not repeated here. However, a brief summary of the information relevant to this

20 evaluation is provided below and in Table 1.

The COALESC campaign involved 16 flights performed by the BAe-146 aircraft of the Facility for Airborne Atmospheric Measurements over the South-East coast of England and Wales, during February and March 2011. Despite that the main objectives of COALESC focused on stratocumulus clouds, numerous flights also involved direct measurements of PSDs within

mixed-phase and cirrus clouds. The instrumentation for cloud particle measurements notably involved the NIXE-CAPS (Novel Ice Experiment - Cloud-Aerosol Spectrometer) (Meyer, 2012; Luebke et al., 2016), which provides distributions of the number concentration of particles with sizes from 0.6 to 937 μm. This instrument consists of a combination of the CAS-DPol probe for particles smaller than 50 μm and the Cloud Imaging Probe (CIPg) for particles larger than 15 μm. The in-cloud PSDs are

5 combined from CAS-Dpol (3.0 to 20 μm) and CIPg (> 20 μm). It should be noted that the NIXE-CAPS inlets have been designed to limit the occurrence of shattering effects, which are further reduced through the use of post-processing by inter-arrival time algorithms. Flight details and additional information regarding the NIXE-CAPS instrument and its uncertainties are provided in Costa et al. (2017) and Meyer (2012), respectively.

ML-CIRRUS took place in March and April 2014 over Europe and the North Atlantic. This campaign aimed at investigating

10 nucleation and life cycle processes in cirrus, as well as their impact on climate. The High Altitude and LOng range (HALO) aircraft flew a total of 16 flights, including 40 h dedicated to the remote sensing or in situ measurement of cirrus. Similar to COALESC, cloud particle measurements were performed by the NIXE-CAPS probe. The reader can refer to Luebke et al. (2016) for further details on these measurements during ML-CIRRUS.

ACRIDICON-CHUVA took place in September 2014 over the Amazonian forest with the primary goal to study the role

15 of anthropogenic aerosols on the life cycle of deep convective clouds and precipitation. This campaign involved the HALO aircraft, which performed 13 research flights for a total of 96 h. The cloud particle measurements were performed by the NIXE-CAPS probe. The algorithms to remove shattered ice fragments were not automatically applied to avoid possible erroneous removal of small droplets in warm and mixed-phase clouds. However, applying the inter-arrival time algorithms generally only negligibly change the cirrus ice particle concentrations, since in cold cirrus the crystals in most cases does not grow to sizes

20 that are subject to shattering. Further details on the use of NIXE-CAPS during ACRIDICON-CHUVA can be found in Costa et al. (2017).

The ATTREX-2014 mission took place between February and March 2014 over the West tropical Pacific. Six flights were performed by the NASA Global Hawk aircraft, for a total of 34 h of measurements inside cirrus within the tropical tropopause layer (TTL, i.e. from an altitude of about 14 to 19 km). During this campaign, PSD measurements were obtained from a Two-

25 Dimension Stereo (2D-S) probe (Lawson et al., 2006) for particle sizes between 5 and 3205 μm (with a maximal bin resolution of 10 μm) and by a Fast Cloud Droplet Probe (FCDP) for sizes from 1 to 50 μm. The 2D-S was specifically developed to limit ice shattering through probe inlet design and is combined with a post-processing treatment based on an inter-arrival time algorithm (Lawson, 2011). The FCDP also is considered to be efficient at removing shattered particles (McFarquhar et al., 2007). These two instruments are therefore combined here to improve the description of small particles in PSD measurements.

30 The FCDP is used to provide the concentration of particles from 3 to 24 μm (i.e. 10 bins) and the 2D-S is used from 25 (i.e. its 3rd bin) to 3205 μm. The 1 μm gap is accounted for by scaling the concentration of the last FCDP bin. More information on 2DS and FCDP measurements during ATTREX-2014 can be found in Thornberry et al. (2017).

SPARTICUS was operated as part of the Atmospheric Measurement and Radiation (ARM) aerial program (Schmid et al., 2013) to reach a better understanding of small ice particles in clouds. This mission took place between January and June 2010

35 over Central USA and involved a Learjet-25 aircraft that performed 200 h of scientific flights in synoptic and convective ice

clouds. Its instrumentation involved the 2D-S probe for particle size measurement. A Forward Scattering Spectrometer Probe (FSSP) was also available during the campaign but its measurements are not included here due to likely contamination by shattering (Field et al., 2003; McFarquhar et al., 2007; Jackson et al., 2015). An advantage of SPARTICUS for this study is that it contains numerous coincident flights with the A-Train, as detailed in Deng et al. (2012).

5 ### 3.2.2 Data processing

In order to ensure an optimal consistency between the PSD measurements from each airborne campaign, an identical post-processing procedure has been followed to treat 1-Hz measurements from the 2DS, FCDP-2DS and NIXE-CAPS. This section discusses the most important details regarding the treatment of these measurements.

First, the 1-Hz measurements have been averaged into 10-s period to improve the statistical reliability of cloud sampling by
10 in situ probes. This averaging also allows for a better comparability with cloud volumes sampled by CloudSat (and therefore DARDAR products), which has an along- and across-track horizontal resolution of 1.7 and 1.4 km, respectively. Considering the average true air speeds (TAS) for each campaign (see Table 1), 10-s PSDs are representative of flight legs from about 1.6 to 2.1 km.

Furthermore, to avoid possible ambiguities and uncertainties related to satellite retrievals and in situ measurements in mixed-
15 phase clouds, this study focuses purely ice clouds, i.e. with a temperature $T_c < -40°C$. However, to allow for additional flexibility in the evaluation, all in situ measurements obtained when $T_c < -30°C$ are considered. Possible contamination by liquid drops are expected to be negligible at these temperatures (Costa et al., 2017).

Finally, the IWC corresponding to each in situ PSD is required to obtain predictions by D05. Bulk measurements are available for SPARTICUS and ATTREX but the bulk IWC was not measured for ACRIDICON-CHUVA, COALESC and ML-CIRRUS.
20 Alternatively, and consistently with Krämer et al. (2016), the m-D relation by Luebke et al. (2016), noted $m_{L16}(D)$, can instead be utilized to estimate IWCs from the NIXE-CAPS PSD measurements. $m_{L16}(D)$ is based on a m-D relation by Mitchell et al. (2010), which was slightly modified to improve the representativeness of the mass concentration for small ice crystals. The validity of this type of approach, and of $m_{L16}(D)$ in particular, was recently consolidated by Erfani and Mitchell (2016) and Afchine et al. (2017), who demonstrated their accuracy and generalizability for all types of ice clouds from $T_c < -20°C$. Because
25 Mitchell et al. (2010) and Erfani and Mitchell (2016) developed and tested their m-D relation using 2D-S measurements from tropical and mid-latitude campaigns (including SPARTICUS), $m_{L16}(D)$ should as well be applicable to SPARTICUS and ATTREX2014. Therefore, for the sake of consistency, $m_{L16}(D)$ is here utilized to estimate the IWC for all campaigns. The uncertainties arising from using a m-D relation are discussed in Erfani and Mitchell (2016) and appear reasonable in the context of this evaluation due to the relatively small sensitivity of D05 predictions to IWC, as discussed in Sec. 4.1.
30 Overall, more than 40 000 PSDs, or 110 h of equivalent cloud sampling, are used for the evaluation presented in this study. These numbers are summarized in Table 1.

3.3 Discussion on the integration threshold

To ensure a consistency with DARDAR when inferring N_i from Eq. (5), the PSD parameters α and β are set to -1 and 3, respectively. However, $\alpha = -1$ implies a discontinuity in $N(D_{eq})$ when the diameter equals zero. An analytic solution for N_i can therefore only be obtained by considering a minimum diameter, D_{min}, for the integral. This threshold must here be

5 chosen within the validity range of the in situ measurements used for the evaluation. As mentioned in Sec. 3.2.1, the 2DS, FCDP and NIXE-CAPS have a different sensitivity to small particles. The former instrument measures ice crystals with sizes down to about $5\,\mu$m, whereas the two latter can detect particles down to $1\,\mu$m. For consistency reasons, and to avoid possible contamination by aerosols, only ice crystal larger than $5\,\mu$m will here be considered when computing N_i from each probe. The same threshold is thus applied when computing N_i from DARDAR.

10 The following results will therefore mostly focus on the concentration in crystals larger than $D_{min} = 5\,\mu$m, noted $N_i^{5\,\mu m}$. Nevertheless, the concentration in particles larger than 25 and $100\,\mu$m, respectively noted $N_i^{25\,\mu m}$ and $N_i^{100\,\mu m}$, will also be used during this evaluation. The $25\,\mu$m threshold corresponds to ice crystals of moderate sizes for which in situ measurements can be considered of higher confidence (e.g. the first two 2D-S bins are removed). The $100\,\mu$m threshold typically involves measurements where no shattering is expected but also corresponds to sizes for which the D05 parameterization is expected

15 to perform well. It is worth mentioning that different physical processes are likely to influence N_i depending on the threshold choice. For instance, small particles that are nucleated through homogeneous freezing should dominate $N_i^{5\,\mu m}$, whereas large particles resulting from aggregation processes are likely to influence $N_i^{100\,\mu m}$.

4 In situ evaluation

4.1 Theoretical capability to predict N_i

20 This section investigates the ability of the PSD parameterization by D05 to predict N_i. PSD predictions are computed on the basis of IWC and N_0^* corresponding to each of the 40 000 PSDs composing the dataset described in Sec. 3.2. Comparing these predictions to the in situ PSDs should provide insights on the accuracy of subsequent N_i values to be expected from D05 in case of optimal retrievals (i.e. when IWC and N_0^* are perfectly constrained).

4.1.1 Reproducibility of PSDs by D05

25 As indicated in Sec. 2.2, the D05 parameterization predicts PSDs based on the assumption of a "universal" size distribution shape and the knowledge of two scaling parameters. Following this formalism, a PSD prediction by D05 can be obtained given the D_m and N_0^* values corresponding to each measured PSD. D_m can directly be extracted from in situ PSDs, as it corresponds to the ratio of $\mathcal{M}_4$ to $\mathcal{M}_3$. N_0^* can be indirectly estimated from D_m and the IWC, using Eq. (9). It can be noted that N_0^* is proportional to $\text{IWC} \times D_m{}^{-4}$, which means that predictions by D05 are much more sensitive to D_m than to the IWC. This point

30 makes the use of $m_{L16}(D)$ to estimate IWC a reasonable approximation for the purposes of this evaluation. The size dimension of PSDs predicted by D05 has been converted from D_{eq} to D to improve the clarity of the following comparisons.
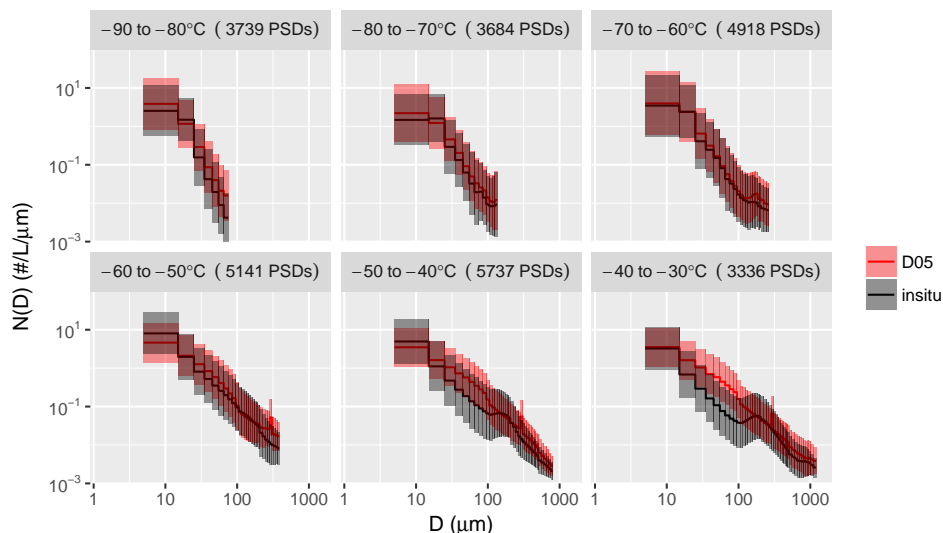
Figure 1. Mean PSDs measured during ATTREX and SPARTICUS (black lines), averaged per 10°C temperature bins (from -90 to -30°C). Black contours indicate one standard deviation around the mean. The mean and spread of one-to-one predictions by the D05 parameterization are similarly indicated by red lines and contours, respectively. The total amount of PSDs in each temperature bin is indicated in the legend.
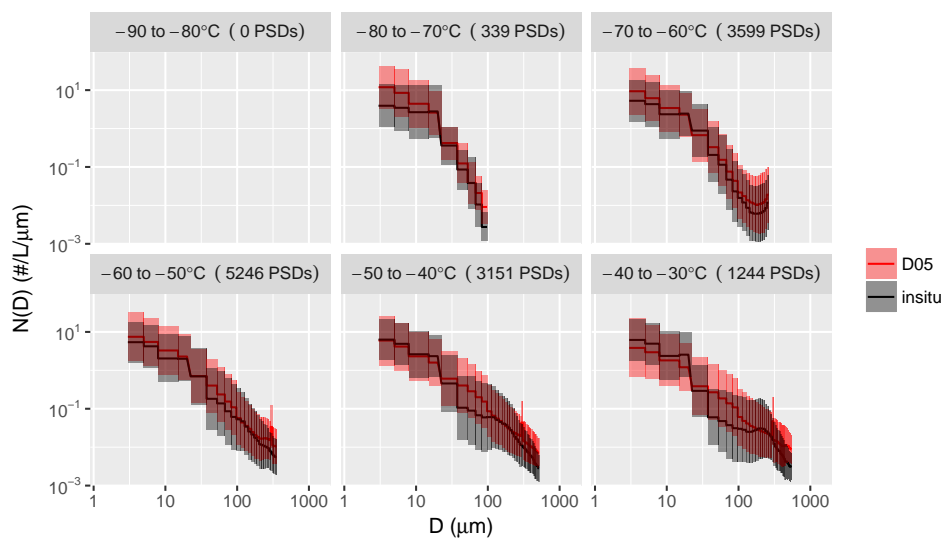
Figure 2. Similar to Fig. 1, for the ACRIDICON-CHUVA, ML-CIRRUS and COALESC campaigns.

Comparisons between the PSD measurements obtained during ATTREX2014 and SPARTICUS and corresponding predictions by D05 are shown in Fig. 1. The black and red lines respectively indicate the mean measured and predicted PSDs within 10°C temperature bins. The use of measurements from mid-latitude (SPARTICUS) and TTL ice clouds (ATTREX2014) allows a high statistical significance to be reached (over 3000 PSDs) in each T_c bin from -90 to -30°C. The colored contours indicate
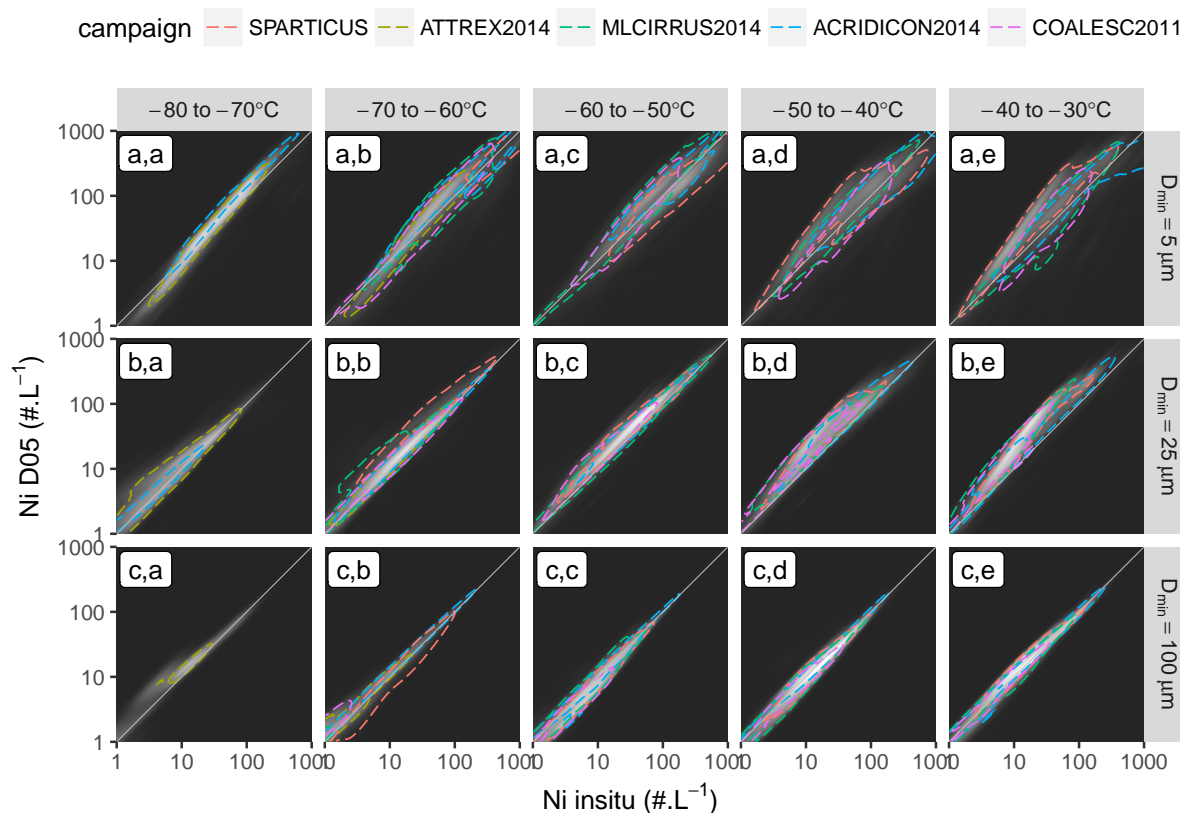
Figure 3. Density scatterplot showing N_i theoretically estimated by D05 as function of corresponding in situ measurements (from white to black indicates high to low frequency of occurrence). Color isolines indicate the 68% (one standard deviation) confidence interval for each campaign. Density and confidence intervals are provided per 10°C temperature bins from -80 to -30°C (first to fifth column) and lower integration threshold for N_i (5, 25 and 100 μm in the first, second and third row, respectively).

one standard deviation around that mean. It can be noted that the measured and predicted concentrations in the FCDP bins have been averaged within each of the two first 2D-S bins in order to conveniently display the means in Fig. 1. This figure clearly shows a very good overall agreement between D05 predictions and the in situ measurements. The mean as well as the spread of the 2D-S and FCDP measurements are well represented by D05. The agreement is especially good for -90°C < T_c < -50°C, where the in situ distribution tends to be mono-modal with very few large particles. However, an overestimation of the number of particles with $D < 100 \mu$m is noted for D05 from T_c > -50°C, where a second mode appears for large aggregated particles. Such features and temperature dependency of PSD shapes have already been widely reported in the literature (e.g. Mitchell et al., 2011; Mishra et al., 2014; Luebke et al., 2016). In the occurrence of a bi-modal shape in in situ measurements, the D05 parameterization naturally tends to reproduce the concentration in large particles due to their strong weight on D_m and IWC. Because a monomodal shape is assumed to describe the PSD in D05, an erroneous extrapolation of the concentration in

small particles leads to the observed overestimation when $T_c > $ -50°C. However, this overestimation appears to mainly concern particles from 25 to 100 μm, as the concentration in ice particles smaller than about 15 μm seems accurately predicted (keeping in mind that measurements for such small particles can be highly uncertain).

These results are supported by the evaluation of the D05 predictions of NIXE-CAPS measurements during ACRIDICON-CHUVA, COALESC and ML-CIRRUS, which are similarly shown in Fig. 2. Despite much fewer measurements of ice clouds with $T_c < $ -70°C, very good agreements are found in the mean and the spread predicted by D05 for -50 $< T_c < $ -70°C. A slight overestimation of the concentration of small ice crystals is found between -80 and -70°C, as the concentration keeps increasing in D05 towards small diameters but not for the NIXE-CAPS. This feature should nevertheless be carefully accounted for due to the lack of measurements in this temperature bin. Consistent with the previous results, the D05 predictions are less accurate towards higher temperatures as bi-modal structures tend to appear in the in situ measurements above -50°C. Moreover, comparing Fig. 2 with Fig. 1 shows a very good overall agreement between the NIXE-CAPS and 2D-S/FCDP measurements, which points towards the generalization of these conclusions. It should be mentioned that these analyses are not repeated by explicitly discriminating between cloud types (e.g. synoptic cirrus/anvil or liquid/ice origin) for reasons of brevity. The overall agreements observed in Fig. 1 and Fig. 2 are considered satisfactory in this evaluation, especially since DARDAR does not discriminate between cloud types and the normalized size distribution used in D05 is expected to perform equally for all cloud types.

4.1.2 Consequences on N_i predictions

N_i obtained from direct integrations of the measured and predicted PSDs are now compared. Fig. 3 shows a density scatterplot of one-to-one comparisons between the in situ measurements (x-axis) and corresponding D05 predictions (y-axis), obtained by integrating the corresponding PSDs from $D_{min} = 5$, 25 and 100 μm (first to third row, respectively). The background color indicates the overall density and isolines are provided to show the 68% confidence levels (i.e. from which all values inside fall within one standard deviation σ from the mean) for each campaign. These results are shown per 10°C temperature bins from -80°C to -30 °C (first to fifth column, respectively).

Fig. 3(c,a-e) show that the prediction of N_i for ice particles larger than 100 μm is very consistent with the in situ truth, with an agreement close to the one-to-one line for all campaigns and temperatures. $N_i^{100\,\mu m}$ values ranging between about 1 and 100 L^{-1} are observed. This good agreement was expected from Sec. 4.1.1, and because D05 should in principle perform best at reproducing the concentration in large particles. Fig. 3(b,a-e) also indicates an accurate prediction of $N_i^{25\,\mu m}$ from -80 to -50°C. However, at higher temperatures, $N_i^{25\,\mu m}$ predictions by D05 are overestimated by a factor of 2 to 3 for most field campaigns. These results also hold for $N_i^{5\,\mu m}$, as indicated in Fig. 3(a,a-e), despite a larger spread within and between the campaigns in this case. It can be noted that the overestimation is particularly strong for SPARTICUS (red isolines) but is less clear for other campaigns. The overestimation is not as clear as for $N_i^{25\,\mu m}$, as the concentration of particles smaller than 25μm appears more properly predicted by D05, as shown in Fig. 1 and Fig. 2. At $T_c < $ -50°C, the D05 predictions are consistent with the in situ measurements, with maximal $N_i^{5\,\mu m}$ values of about 300 L^{-1} but that can also reach up to 1000 L^{-1} for several field campaigns.
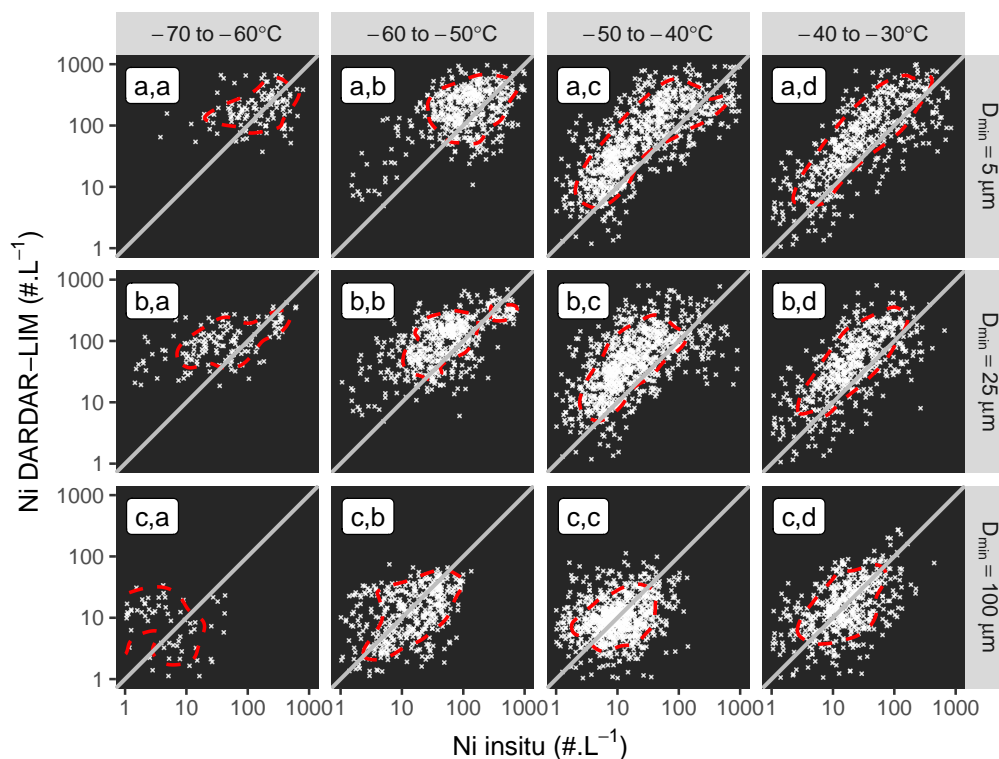
Figure 4. Similar to Fig. 3, scatterplots of N_i retrieved by DARDAR-LIM as function of the co-incident in situ SPARTICUS measurements.

4.2 Satellite estimates vs. co-incident measurements

The theoretical ability of the D05 parameterization to predict N_i measurements from numerous airborne campaigns was demonstrated in Sec. 4.1. However, these conclusions only reflect ideal cases, where the input parameters of this parameterization are perfectly known. In other words, they correspond to the expectations for retrievals where the lidar and/or radar information are capable of perfectly constraining these parameters. It is now necessary to investigate if enough information is contained in these measurements to constrain D_m and N_0^* so that N_i is well estimated.

This question is investigated by comparing the DARDAR-LIM N_i to measurements from co-incident flights. These flights are selected under the condition that they are within a maximum distance of 5 km and a 30-min time period from the Cloud-Sat/CALIPSO overpass. Among the campaigns described in Sec. 3.2.1, co-incident flights with the A-Train track were intended during ACRIDICON-CHUVA, ML-CIRRUS and SPARTICUS. Unfortunately, none of the 3 co-incident flights during ACRIDICON-CHUVA could be selected here, due to the absence of CALIOP measurements (12 Sept. 2014) or flights that do not fulfill the above conditions (about 3 h late or 350 km West from the overpass track on 21 and 23 Sept. 2014, respectively). Also, technical issues occurred during the ML-CIRRUS co-incident flights (04 April 2014), making PSD measurements uncertain and not usable for this evaluation. However, numerous flights successfully achieved a close spatial and temporal co-
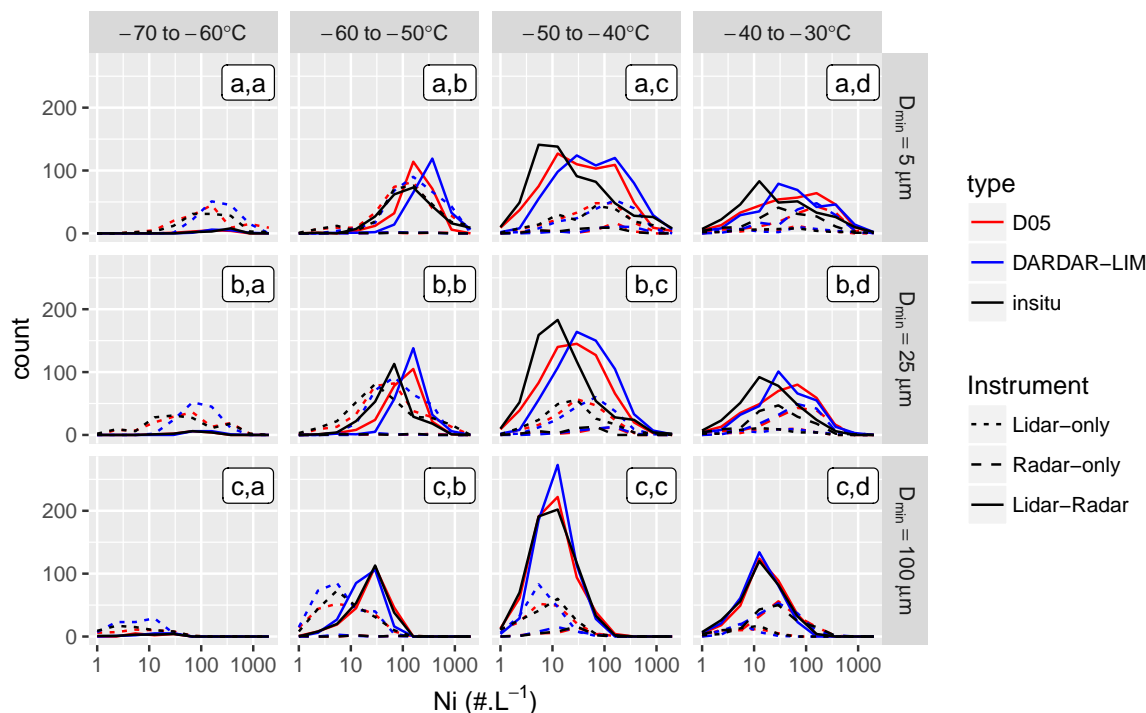
Figure 5. Histograms of N_i measured during SPARTICUS (black), theoretically estimated by D05 (red) and retrieved by DARDAR-LIM (blue). Plain, dotted and dashed lines indicate that DARDAR retrievals were obtained using the lidar-radar, lidar-only, radar-only, respectively. Panels indicate the temperature and integration threshold, similarly to Fig. 3

.

incidence with the A-Train during SPARTICUS. A list and description of all these flights can be found in Deng et al. (2012). Overall, about 2150 PSDs were here found to match the above conditions and are considered in this evaluation. The co-incident DARDAR-LIM N_i are obtained by selecting the closest pixel (based on a great-circle distance) at the altitude of the airplane.

Figure 4 shows, similarly to Fig. 3, scatterplots of the DARDAR-LIM N_i as function of co-incident 2D-S measurement for the

5 three considered D_{min} thresholds and four T_c bins from -70 to -30°C. It can first be observed that these comparisons are rather widely scattered, as could be expected due to the difficulty of performing one-to-one comparisons between satellite and airborne measurements. Nevertheless, the $N_i^{100\,\mu m}$ is in good overall agreement. In spite of the large scatter, the isoline representative a 1-σ spread (dashed red) is centered around the one-to-one line. However, a clear tendency towards an overestimation of N_i when $T_c \gtrsim$ -50°C is observed for $N_i^{5\,\mu m}$ and $N_i^{25\,\mu m}$. For colder temperatures, the DARDAR-LIM N_i estimates are in much

10 better agreement with the SPARTICUS measurements. Despite the larger scatter, these results are consistent with expectations from Sec. 4.1.2.

In order to avoid problems related with one-to-one comparisons of satellite and airplane measurements, a statistical comparisons is presented in Fig. 5. This figure shows histograms of N_i distributions for the 2D-S (black) and DARDAR-LIM (blue)

per temperature bin and D_{min} threshold. Additionally, the theoretical prediction by D05 (obtained using the in situ D_m and N_0^*) also is indicated in red to provide an idea of the optimal expectations from D05. Plain, dotted and dashed lines indicate satellite estimates that were obtained using the lidar-radar, lidar-only, radar-only measurements, respectively. Fig. 5(c,a-d) show a very good agreement between the satellite $N_i^{100\,\mu m}$ in comparison to the in situ observations at all temperature ranges. This agree-

5 ment appears to be equally good for retrievals obtained in lidar-only, radar-only or lidar-radar conditions. Fig. 5(a,a-c) shows that the estimation of $N_i^{5\,\mu m}$ is relatively consistent with the 2D-S observations for $T_c < -50°C$. The expected overestimation for higher temperatures tends is observed, as the DARDAR-LIM histograms appear nearly shifted by a factor of about 2 to 3. It should nevertheless be kept in mind that SPARTICUS featured the strongest biases at these temperature range by comparison to other campaigns, as seen in Fig. 3. $N_i^{5\,\mu m}$ estimates obtained from lidar-only and lidar-radar measurements are all in good

10 agreement, which indicates that reliable N_i estimates can be obtained from any of these combinations. The statistical sampling of retrievals obtained in radar-only condition is too poor to draw any strong conclusions. Finally, it clearly appears from Fig. 5 that, even when the distributions from DARDAR-LIM and the 2D-S do not perfectly agree, the satellite estimates very often remain close to the D05 predictions. Because the latter represent ideal retrievals, this again proves that sufficient information is contained in lidar-radar measurements to successfully constrain the D05 input parameters and estimate N_i.

5 Case study

A first examination of N_i profiles by DARDAR-LIM is performed here in the context of a case study corresponding to a frontal ice cloud structure observed on 03 February 2010 around 20:00 UTC over South Central USA. This case is of particular interest as it contains a leg of high spatial and temporal coincidence between the A-Train and the Learjet-25 aircraft involved during SPARTICUS.

5.1 Overall context

The cloud structure analyzed here is part of a mature cyclonic system that has reached an occluded stage, as featured by the brightness temperature snapshot shown in Fig. 6(a). Further analyses of the weather conditions (not shown here for brevity reasons) indicated that this system originated from a mid-tropospheric wave pattern that crossed the US and supported a surface low pressure area over North Central Mexico. The storm then moved northwesterly, eventually reaching Northeastern USA on

25 05 February as a major blizzard.

The CloudSat track crossed the cyclone from south to north around 19:55 UTC (dashed green line). The section of interest for this case study (plain green line) captures a frontal cloud associated with the ascending southern moist warm air flow atop cold continental air mass. The corresponding CloudSat Z_e and CALIOP β_{ext} profiles, shown in Fig. 7(a-b), typically hint to high water contents and precipitation toward the center of the cyclone and to thin ice clouds as the A-Train moves northwards

30 toward its periphery.

The Learjet-25 performed in situ measurements in a cirrus at the edge of the cyclone. The flight track is shown by black lines in Fig. 6(a-b) and Fig. 7. These figures indicate that the aircraft approached from the west at an altitude of about 10.7 km (near
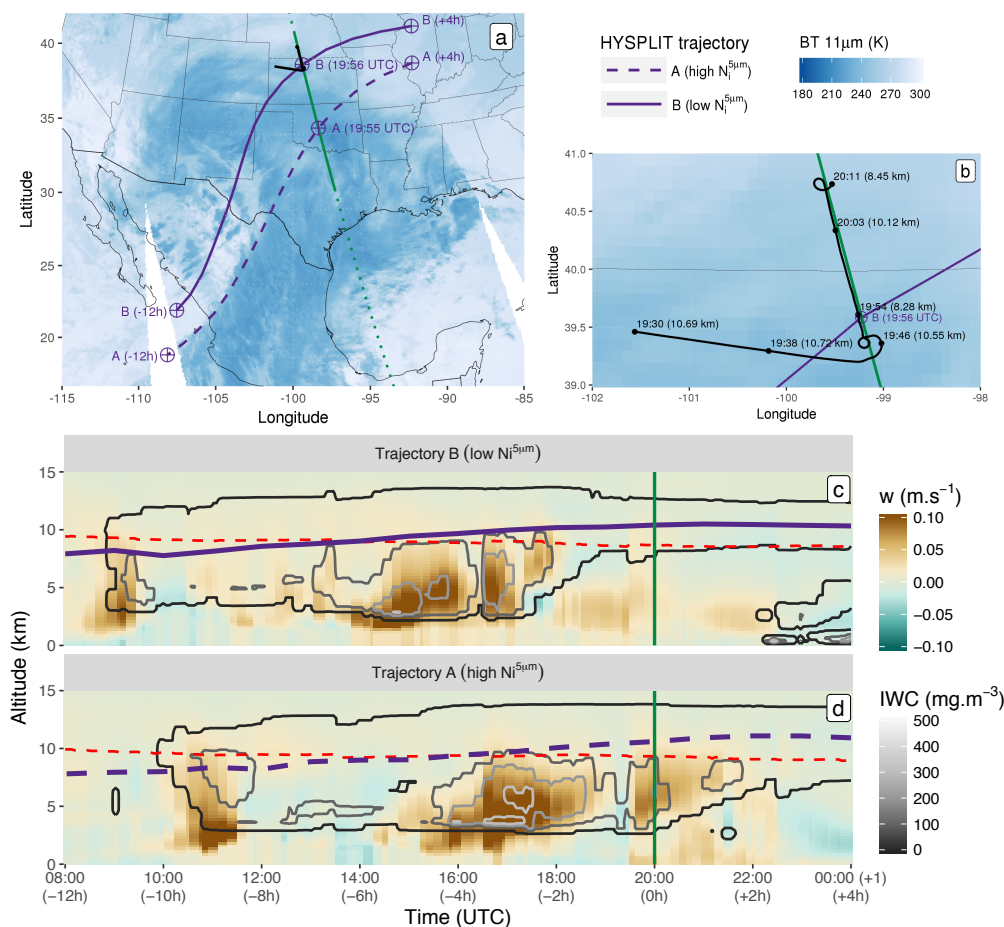
Figure 6. (a): Map summarizing the observations during the case study. The shaded blue background corresponds to MODIS/Aqua 11 μm brightness temperature measurements around the A-Train overpass. The CloudSat track is shown by a dotted green line and a plain green line highlights the region of interest. The Learjet-25 flight track is shown in black. Dashed and plain purple lines represent HYSPLIT trajectories computed for 2 air parcels of high (A) and low (B) $N_i^{5\,\mu m}$, respectively, at 11 km along the overpass. (b): Similar to (a) but zoomed in around the flight area. The aircraft UTC times and altitudes are indicated in black. (c-d): Vertical cross sections of w (background color) and IWC (grey contours) predicted by NARR along the B and A trajectories, respectively. The positions of the corresponding air parcel are indicated in purple. A dashed red line shows the -40 °C isotherm. The overpass time is highlighted by a vertical green line.

cloud top) and descended to about 8 km (near cloud base) before reaching the overpass. The aircraft then closely followed the A-Train while ascending to cloud top and finally descended back to cloud base in a spiral. Optimal comparisons between the A-Train and Learjet-25 measurements are thus expected within the ascending leg from about 39.5 to 40.7°N, where the time and space coincidences are well within 15 min and 10 km, respectively.
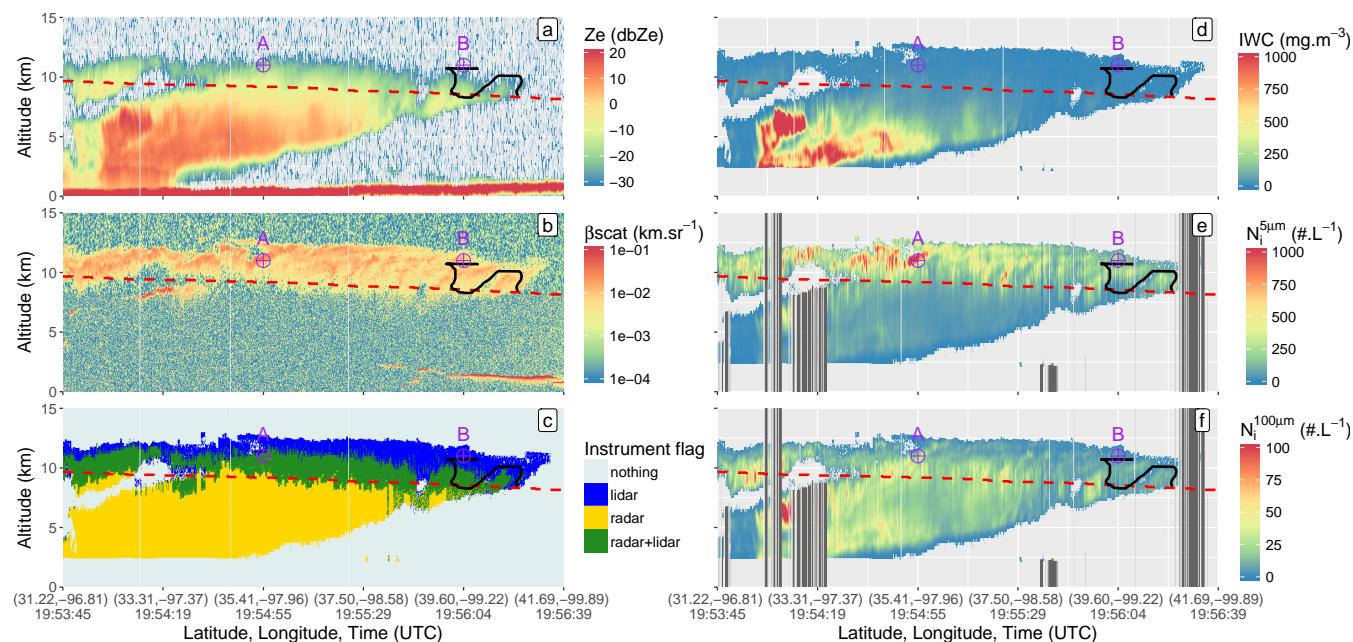
Figure 7. Vertical profiles of the (a) CloudSat reflectivity factor, (b) CALIOP backscatter coefficient, (c) DARDAR instrument flag, (d) DARDAR IWC, (e-f) DARDAR-LIM $N_i^{5\,\mu m}$ and $N_i^{100\,\mu m}$, respectively, along the selected A-Train overpass (plain green line in Fig. 6). Dark-grey shaded areas in (e-f) indicate a rejection of the retrievals (insufficient n_{iter} or the below a supercooled layer; see Sec. 3.1). The -40°C isotherm is in dashed red, the location of the A and B air parcels are indicated in purple, and the Learjet-25 track is shown in black.

5.2 Vertical structure along the overpass

Profiles of IWC, $N_i^{5\,\mu m}$ and $N_i^{100\,\mu m}$ along the selected A-Train overpass are respectively shown in Fig. 7(d-f). As expected, high IWC values are retrieved between altitudes of 2.5 and 7.5 km along the southern half of the track (31.2-35.4°N), i.e. towards the center of the cyclone. The clear cut below 2.5 km, associated with high Z_e, corresponds to pixels classified as rain by the

5 DARDAR mask. Fig. 7(e) shows that large $N_i^{5\,\mu m}$ values are found towards cloud top, with values ranging from 250 to more than 1000 L^{-1}. $N_i^{5\,\mu m}$ strongly increases above the -40° isoline (dashed red line), consistently with the probable occurrence of homogeneous nucleation below that temperature threshold. However, the increase in $N_i^{5\,\mu m}$ when $T_c < $ -40°C is not spatially homogeneous. Indeed, very high values (reaching 1000 L^{-1}) are observed between 33.3 and 36.5°N, where the cloud-base heights starts increasing in relation with the frontal system. However, lower $N_i^{5\,\mu m}$ with values, typically between 250 and

10 500 L^{-1}, are observed above -40°C toward the cyclone periphery (36.5 to 41.5°N). This distribution of $N_i^{5\,\mu m}$ is consistent with expectations of stronger updraughts and vertical transport of moisture closer to the center of the cyclone, resulting in higher homogeneous nucleation rates by comparison to a more mature stage of the cloud (Krämer et al., 2016). This hypothesis will further be discussed in Sec. 5.3.

Vertical profiles of $N_i^{100\,\mu m}$ are shown in Fig. 7(f). It is observed that areas of high $N_i^{100\,\mu m}$ are located deeper in the cloud than where high $N_i^{5\,\mu m}$ are found. $N_i^{100\,\mu m}$ tends to increase below regions of high $N_i^{5\,\mu m}$, which is coherent with possible aggregation processes, and remains constant or decreases slightly towards cloud base before precipitating from the lowermost layers. Very high $N_i^{100\,\mu m}$ values appear around 33.0°N, coincident with high IWC values. However, Fig. 7(b) shows the

5   presence of a supercooled cloud layer in this area, typically below an area of high backscatter coefficient at high altitude, where retrievals are highly uncertain. It is worth noting that the $N_i^{100\,\mu m}$ distribution does not necessarily follows that of the IWC.

Furthermore, comparing the N_i profiles in Fig. 7(e-f) with the corresponding instrumental flags shown in Fig. 7(c) indicates that no clear bias is observed within transition areas between the cloud properties obtained in lidar-only, radar-only and lidar-

10   radar conditions, confirming the conclusions from Fig. 5.

Finally, comparisons between DARDAR-LIM and coincident 2D-S measurements are presented in Fig. 8. The method for co-locating and comparing aircraft and satellite observations is identical to that used in Sec. 4.2, except that no filters based on the coincidence distance and time are applied here. Overall, this figure shows very similar $N_i^{5\,\mu m}$ and $N_i^{100\,\mu m}$ patterns between the satellite estimates and the in situ measurements, with especially good agreements along the ascending leg corresponding to

15   the optimal coincidence region (39.5-40.7°N). Few discrepancies are nevertheless observed outside this region. For instance, DARDAR-LIM does not capture well the sporadic strong increases of $N_i^{5\,\mu m}$ observed above 10 km, which however corresponds to measurements where the aircraft largely deviated from the A-Train track (western leg in Fig. 6(b)), and slightly overestimates $N_i^{5\,\mu m}$ along the descending leg around 40.75°N. Also, the increase in $N_i^{100\,\mu m}$ observed by the 2D-S along the descending leg around 39.4°C is well not captured by the satellite, possibly because of a movement of the cloud layer or a slight

20   difference in the co-location (Fig. 7(f) indicates $N_i^{100\,\mu m}$ values between 25 and 50 L^{-1} next to the aircraft track). However, accounting for the difficulties to directly compare aircraft and satellite observations, it can be concluded here that DARDAR-LIM reproduces reasonably well the average values and variations of the $N_i^{5\,\mu m}$ within this cloud layer, thus supporting the conclusions drawn from Sec. 4.2.

5.3 Trajectory analysis of $N_i^{5\,\mu m}$ patterns

25   Thorough investigations of nucleation processes based on DARDAR-LIM are not in the scope of this paper and will further be discussed in the part two of this series. Nevertheless, a qualitative analysis is here presented to provide further explanation to the $N_i^{5\,\mu m}$ patterns observed in this case study.

To achieve this, back- and forward-trajectories were computed from the points A and B indicated in Fig. 7, using the Hybrid Single Particle Lagrangian Integrated Trajectory Model (HYSPLIT; Stein et al., 2015) coupled with the North American

30   Regional Reanalysis (NARR; Mesinger et al., 2006) model. A and B correspond to air parcels associated with high and low $N_i^{5\,\mu m}$, respectively, when $T_c < -40$°C. Their trajectories (from -12 to +4 h starting at the overpass time) are shown as dashed and plain purple lines, respectively, in Fig. 6(a). The corresponding altitudes are similarly indicated as function of time in Fig. 6(c-d). Complementarily, the vertical cross-sections of vertical wind velocities (w) predicted by NARR along the trajectories are indicated by a color background in Fig. 6(c-d). Contours of the NARR IWC are shown in grey to serve as rough indicators of
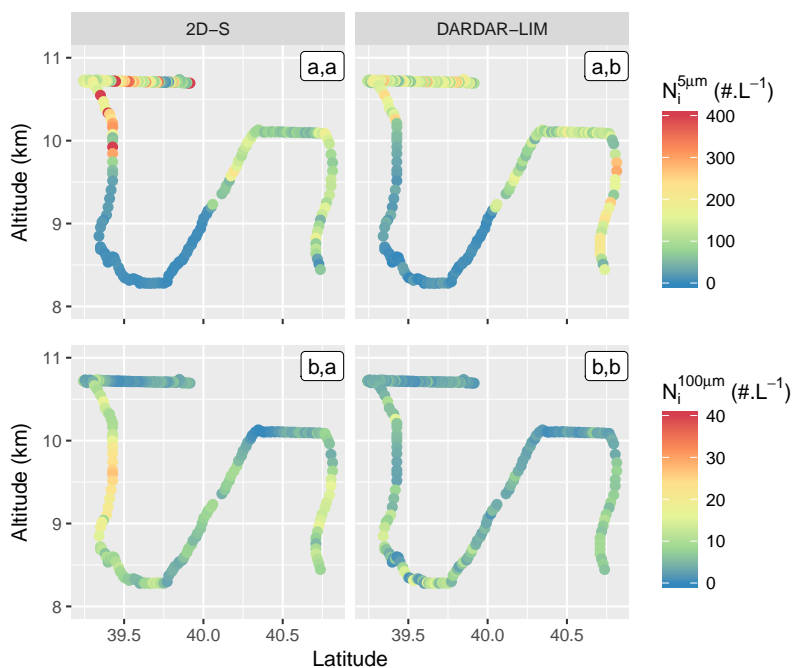
Figure 8. (a,a-b) $N_i^{5\,\mu m}$ measured by the 2-DS and retrieved by DARDAR-LIM, respectively, along a projection of the Learjet-25 track on the A-Train overpass. (b,a-b) Similar to previous but for $N_i^{100\,\mu m}$.

the presence of ice cloud layers in the model. It can be noted that NARR provides reanalyses with an horizontal resolution of 32 km, 29 vertical levels and with 3-hourly outputs; the closest output times and grid-points were therefore selected.

It is observed that, in agreement with expectations, both air parcels originated from warm moist air over the Pacific and slowly ascended atop the cold continental air following northwesterly trajectories associated with slow vertical motions (light brown colours). Parcel B ascended from about 8 km at 08:00 UTC to 11 km at the overpass time (20:00 UTC) and then remained at a constant altitude. The -40°C isoline (dashed red line) is crossed around 14:00 UTC and this parcel then appears to belong to an anvil-like maturing cloud layer from 19:00 UTC, supported by small w observed around the overpass time. On the contrary, parcel A, which also started ascending from an altitude around 7.5 km, met strong convective events later during the day, around 16:00 UTC. Consistently, the -40°C isoline is also crossed about 2 h later than for parcel B. This parcel keeps ascending upon meeting with the overpass, where strong updraughts are still indicated.

These observations are in agreement with the high $N_i^{5\,\mu m}$ values observed at A, thus likely to be caused by strong and recent updraughts that carry moisture above the -40°C isotherm and allow for high homogeneous nucleation rates. This is consistent with a very strong sensitivity of N_i to w (Krämer et al., 2016). On the contrary, B corresponds to an air parcel within a mature cloud, where w is too small to cause further ice nucleation and small ice crystals have already started to sublimate or aggregate. Keeping in mind possible uncertainties associated with the NARR reanalyses and HYSPLIT trajectories, this analysis still provides comforting arguments as to physical meaningfulness of $N_i^{5\,\mu m}$ patterns in DARDAR-LIM.
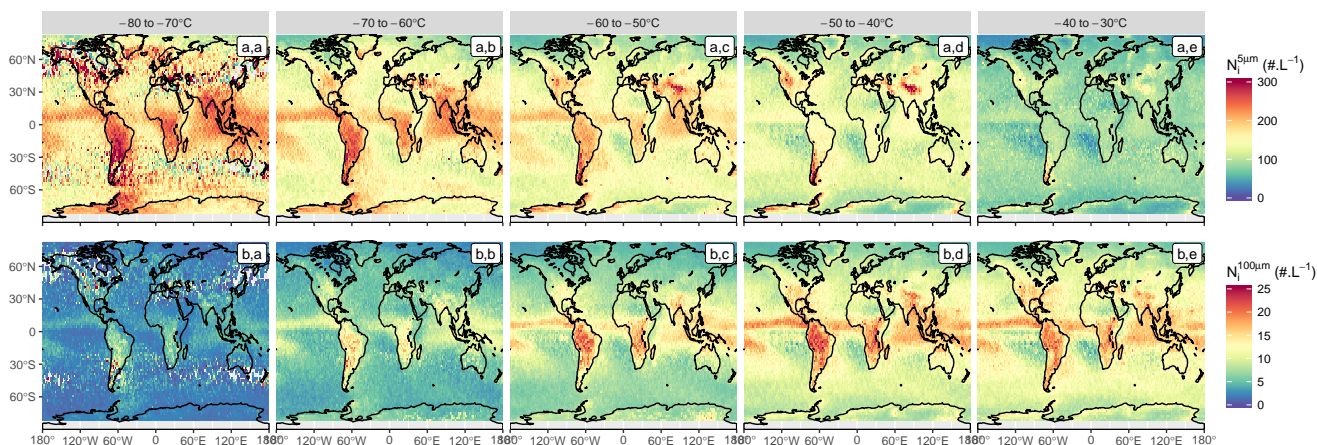
Figure 9. Spatial distribution of $N_i^{5\,\mu m}$ (a,a-e) and $N_i^{100\,\mu m}$ (b,a-e) from 2006 to 2016, averaged in a $2 \times 2°$ lat-lon grid and per 10°C temperature bin from -80 to -30°C.

6 Preliminary evaluation of N_i climatologies

Spatial distributions of $N_i^{5\,\mu m}$ and $N_i^{100\,\mu m}$ corresponding to 10 years of DARDAR-LIM products are now analysed. A thorough evaluation of these distributions remains difficult due to a lack of other reference for such climatological data; preliminary results are thus discussed here to assess the overall coherence of the observed N_i patterns with general expectations but should

5   be cautiously considered. The interpretation of these distributions in terms of evidence of controls on N_i are here only briefly addressed as they will be the focus of part two.

6.1 Global spatial distributions

Figures 9(a,a-e) show the spatial distribution of $N_i^{5\,\mu m}$ averaged in a $2 \times 2°$ lat-lon grid and subset into 10°C bins from -80 to -30°C. The $N_i^{5\,\mu m}$ shows a strong temperature dependence, with higher $N_i^{5\,\mu m}$ values being observed at colder T_c globally

10   (Fig. 9(a,a-e)). This T_c dependence is particularly strong over tropical land regions and in regions experiencing strong convection (the tropical warm pool, intertropical convergence zone). This is consistent with the strong updraughts in convective regions producing high supersaturations and so higher nucleation rates, causing these increased $N_i^{5\,\mu m}$ values (Kärcher and Lohmann, 2002; Krämer et al., 2016).

    There is also a strong T_c relationship in orographic regions, but it is prominent at warmer temperatures, with a large increase

15   in $N_i^{5\,\mu m}$ being observed in the Himalayas, the Rockies, Southern Andes and the Antarctic Peninsula, as well as the edge of the East Antarctic icesheet (Fig. 9(a,d)). These higher $N_i^{5\,\mu m}$ values are typically found in the mid-latitudes, where higher windspeeds provide stronger orographic uplifts (Gryspeerdt et al., 2017). Consequently, such features are less likely in the tropics, where the atmosphere is barotropic. This is for instance clearly noted in the Andes, where no high $N_i^{5\,\mu m}$ values appear at the northern end.
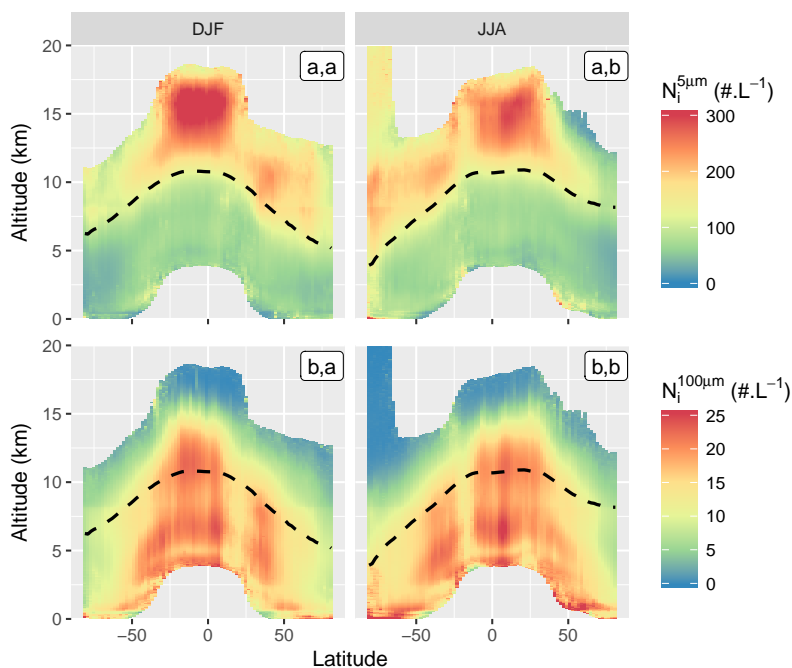
Figure 10. Zonal profiles of $N_i^{5\,\mu m}$ (a,a-b) and $N_i^{100\,\mu m}$ (b,a-b), during northern hemisphere winter (a-b,a) and summer (a-b,b) seasons.

The spatial distribution of the $N_i^{100\,\mu m}$ shown in Fig. 9(b,a-e) is noticeably different, with a significantly reduced $N_i^{100\,\mu m}$ at lower temperatures. This might be expected through the reduced efficiency of the aggregation and deposition processes needed to generate larger crystals at colder T_c, along with the size-sorting of ice crystals in cirrus clouds. At all the temperatures examined, higher $N_i^{100\,\mu m}$ values are observed in convective regions, where updraughts are sufficient to transport large particles to the upper troposphere, but also where high $N_i^{5\,\mu m}$ at colder temperatures subsequently lead to high $N_i^{100\,\mu m}$ as the clouds mature.

These spatial distributions agree with recent studies showing the distribution of nucleation rates and N_i based on global modeling (e.g. Gasparini and Lohmann, 2016; Barahona et al., 2017), although detailed comparisons are out of the scope of this study.

6.2 Zonal profile distributions

Subsets of zonal profiles distributions of $N_i^{5\,\mu m}$ and $N_i^{100\,\mu m}$ corresponding to the northern hemisphere winter (DJF) and summer (JJA) seasons are presented in Fig. 10(a,a-b). As with the global maps in Fig. 9(a,a-e), a strong increase in $N_i^{5\,\mu m}$ is observed at T_c decreases. However, it is clear from these zonal plots that this relationship is not linear, as a strong increase in $N_i^{5\,\mu m}$ is observed around the $T_c = -40°C$ isotherm (dashed line). Because homogeneous nucleation rates become significant at colder temperatures (Koop et al., 2000), this suggests that the $N_i^{5\,\mu m}$ at temperatures colder than -40°C is strongly influenced by homogeneous nucleation processes. This increase in $N_i^{5\,\mu m}$ is particularly strong in the tropics, where strong convective

updraughts may be able to generate the high supersaturations required for homogeneous nucleation. In the mid-latitudes, the temperature dependence is stronger in the winter hemisphere. This may indicate the role of seasonal variations in cloud or aerosol types, a subject that will be explored in more detail in part two. It can also be noted that $N_i^{5\,\mu m}$ values of about $150\,L^{-1}$ are observed above $12\,km$ over the Antarctic during the winter season, possibly related to the presence of polar stratospheric

5 clouds (Noel et al., 2008).

Consistent with the global maps in Fig. 9(b,a-e), there is a strong decrease in $N_i^{100\,\mu m}$ with decreasing temperature. This temperature dependence is much stronger for $T_c < $ -40°C, becoming much weaker at warmer temperatures. Despite being lower than $N_i^{5\,\mu m}$, at warmer temperatures, the $N_i^{5\,\mu m}$ reaches values higher than $20\,L^{-1}$, such that large crystals comprise a significant fraction of the total $N_i^{5\,\mu m}$ (50-100 L^{-1}).

10 ## 7 Summary and conclusions

A novel approach to estimate N_i from combined CALIPSO-CloudSat measurements, called DARDAR-LIM, is here presented and evaluated against in situ measurements and in the context of a case study and a preliminary climatological analysis.

Based on over 40 000 PSD measurements from five recent in situ campaigns, it is demonstrated that N_i can be predicted by constraining the moments of normalized PSDs using β_{ext} and Z_e measurements. The D05 parameterization appears capable of

15 predicting reasonably well the measured concentration of particles from different minimum size thresholds and for ice clouds with T_c spanning from -90 to -30°C, demonstrating good predictions of $N_i^{5\,\mu m}$ and $N_i^{100\,\mu m}$ (Fig. 3). A possible bias in $N_i^{5\,\mu m}$ predictions is nevertheless noted when $T_c \gtrsim$ -50°C and is explained by a misrepresentation in D05 of the bi-modality observed in the measured PSDs (Fig. 1-2). Following these results, it is verified that N_i estimates inferred from IWC and N_0^* retrievals of DARDAR, which uses D05, are also in good agreement with the in situ measuremens from co-incident flights (Fig. 4-5). These

20 comparisons further demonstrate the sufficient sensitivity in β_{ext} and Z_e to constrain N_i. It is also observed that similarly good agreements are found in lidar-only and lidar-radar conditions, while more statistics are required to draw strong conclusions for radar-only condition.

Reasonable physical consistency is also found in the vertical distribution of N_i estimates analysed along a short orbital track in the context of a case study representative of an occluded frontal system. Strong $N_i^{5\,\mu m}$ increases are observed below -40°C

25 (Fig. 7(e)), in conformity with higher homogeneous nucleation rates. Large $N_i^{100\,\mu m}$ values are found deeper in thick cloud layers. As expected, very good consistency is observed between estimates obtained in lidar-only, radar-only and lidar-radar conditions. Based on a quantitative analysis of the trajectory of two air masses, it is observed that regions that are subject to stronger updraughts and therefore supplied moisture show peaks in $N_i^{5\,\mu m}$, whereas regions representative of mature cloud parcels do not. Direct comparisons to aircraft measurements that are co-incident with the satellite track again confirm that

30 DARDAR-LIM reproduces well the overall values and spatial variability measured in situ (Fig. 8).

Finally, global distributions of $N_i^{5\,\mu m}$ and $N_i^{100\,\mu m}$ are analysed on the basis of a 10-year climatology (Fig. 9-10). An overall increase of $N_i^{5\,\mu m}$ with decreasing temperature is observed but its rate is regionally dependent. A global increase is observed as T_c reaches -40°C, consistent with a strong temperature dependency of the homogeneous nucleation rate. However, steep

increases when $T_c < -50°C$ are only observed in regions where uplifts are sustained by convection or orography, in agreement with expectations of high sensitivity of the N_i to updraughts.

The lidar-radar N_i estimates introduced in this study thus constitute a first and very encouraging basis to provide global observational constraints of this quantity, which open the door to a better understanding of cloud processes and their evaluation in climate and numerical weather prediction models. Improvements of the method remain necessary to reduce the uncertainties related to these N_i estimates. In particular, the use of a PSD parameterization that is better fitted to retrieving N_i (i.e. with a better representation of bi-modality) should be implemented. Further comparisons to in situ measurements as well as modeling are also intended to continue to evaluation of this new N_i product. A detailed investigation of the controls on N_i based on the DARDAR-LIM dataset is presented in part two of this series.

Acknowledgements. The DARDAR product was retrieved from the ICARE data center. The authors gratefully acknowledge the science teams involved in collecting and providing the airborne measurements used in this study. The SPARTICUS and ATTREX data were respectively retrieved from the ARM data discovery center and NASA Earth Science Project Office. The authors are grateful to P. Lawson for helpful discussions regarding the processing of 2DS and FCDP data from these two campaigns. NIXE-CAPS measurements for ACRIDICON-CHUVA, COALESC and ML-CIRRUS were provided by AA and MK. The authors acknowledge the NOAA Air Resources Laboratory and National Center for Atmospheric Prediction for the provision of HYSPLIT trajectories and NARR reanalyses. The MODIS MYD09CMG data product was retrieved from the online Data Pool, courtesy of the NASA Land Processes Distributed Active Archive Center (LP DAAC). We are grateful to the Deutsches Klimarechenzentrum (DKRZ) for providing computational resources necessary for this study. This work was funded by the European Research Council (Grant 306284 "QUAERERE"), by the Federal Ministry for Education and Research in Germany (Bundesministerium für Bildung und Forschung, BMBF) in the "HD(CP)[2]" project (FKZ 01LK1210D, 01LK1503A and 01LK1505E) and by the German Research Foundation (Deutsche Forschungsgemeinschaft, DFG) in Priority Programme SPP 1294 "HALO", project QU 311/14-1 ("FLASH"). TG received funding from the European Union Horizon 2020 research and innovation programme under the Marie Sklodowska-Curie Grant Agreement No. 703880. EG was supported by and Impe- rial College London Junior Research Fellowship. We acknowledge support from the German Research Foundation (DFG) and Leipzig University within the program of Open Access Publishing.

References

Afchine, A., Rolf, C., Costa, A., Spelten, N., Riese, M., Buchholz, B., Ebert, V., Heller, R., Kaufmann, S., Minikin, A., Voigt, C., Zöger, M., Smith, J., Lawson, P., Lykov, A., Khaykin, S., and Krämer, M.: Ice particle sampling from aircraft – influence of the probing position on the ice water content, Atmos. Meas. Tech. Discuss., pp. 1–23, https://doi.org/10.5194/amt-2017-373, 2017.

5 Austin, R. T. and Stephens, G. L.: Retrieval of stratus cloud microphysical parameters using millimeter-wave radar and visible optical depth in preparation for CloudSat: 1. Algorithm formulation, J. Geophys. Res. Atmos., 106, 28 233–28 242, 2001.

Austin, R. T., Heymsfield, A. J., and Stephens, G. L.: Retrieval of ice cloud microphysical parameters using the CloudSat millimeter-wave radar and temperature, J. Geophys. Res. Atmos., 114, https://doi.org/10.1029/2008JD010049, 2009.

Barahona, D., Molod, A., and Kalesse, H.: Direct estimation of the global distribution of vertical velocity within cirrus clouds, Scientific

10 Reports, 7, 6840, https://doi.org/10.1038/s41598-017-07038-6, 2017.

Baran, A. J.: A review of the light scattering properties of cirrus, J. Quant. Spectrosc. Radiat. Transfer, 110, 1239–1260, https://doi.org/10.1016/j.jqsrt.2009.02.026, 2009.

Battaglia, A. and Delanoë, J.: Synergies and complementarities of CloudSat-CALIPSO snow observations, J. Geophys. Res. Atmos., 118, 721–731, https://doi.org/10.1029/2012JD018092, 2013.

15 Benedetti, A., Stephens, G. L., and Haynes, J. M.: Ice cloud microphysics retrievals from millimeter radar and visible optical depth using an estimation theory approach, J. Geophys. Res. Atmos., 108, 2156–2202, https://doi.org/10.1029/2002JD002693, 2003.

Bennartz, R. and Rausch, J.: Global and regional estimates of warm cloud droplet number concentration based on 13 years of AQUA-MODIS observations, Atmos. Chem. Phys., 17, 9815–9836, 2017.

Boers, R., Acarreta, J. R., and Gras, J. L.: Satellite monitoring of the first indirect aerosol effect: Retrieval of the droplet concentration of

20 water clouds, J. Geophys. Res. Atmos., 111, 2156–2202, 2006.

Boucher, O., Randall, D., Artaxo, P., Bretherton, C., Feingold, G., Forster, P., Kerminen, V.-M., Kondo, Y., Liao, H., Lohmann, U., Rasch, P., Satheesh, S., Sherwood, S., Stevens, B., and Zhang, X.: Clouds and Aerosols, in: Climate Change 2013: The Physical Science Basis. Contribution of Working Group I to the Fifth Assessment Report of the Intergovernmental Panel on Climate Change, edited by Stocker, T., Qin, D., Plattner, G.-K., Tignor, M., Allen, S., Boschung, J., Nauels, A., Xia, Y., Bex, V., and Midgley, P., 10.1017/CBO9781107415324.016,

25 Cambridge University Press, Cambridge, United Kingdom and New York, NY, USA, 2013.

Brenguier, J.-L., Pawlowska, H., Schüller, L., Preusker, R., Fischer, J., and Fouquart, Y.: Radiative Properties of Boundary Layer Clouds: Droplet Effective Radius versus Number Concentration, J. Atmos. Sci., 57, 803–821, 2000.

Brown, P. R. A. and Francis, P. N.: Improved Measurements of the Ice Water Content in Cirrus Using a Total-Water Probe, J. Atmos. Oceanic Technol., 12, 410–414, 1995.

30 Ceccaldi, M., Delanoë, J., Hogan, R. J., Pounder, N. L., Protat, A., and Pelon, J.: From CloudSat-CALIPSO to EarthCare: Evolution of the DARDAR cloud classification and its comparison to airborne radar-lidar observations, J. Geophys. Res. Atmos., 118, 7962–7981, https://doi.org/10.1002/jgrd.50579, 2013.

Comstock, J. M., Lin, R.-F., Starr, D. O., and Yang, P.: Understanding ice supersaturation, particle growth, and number concentration in cirrus clouds, J. Geophys. Res. Atmos., 113, https://doi.org/10.1029/2008JD010332, 2008.

35 Costa, A., Meyer, J., Afchine, A., Luebke, A., Günther, G., Dorsey, J. R., Gallagher, M. W., Ehrlich, A., Wendisch, M., Baumgardner, D., Wex, H., and Krämer, M.: Classification of Arctic, Mid-Latitude and Tropical Clouds in the Mixed-Phase Temperature Regime, Atmos. Chem. Phys. Discuss., 2017, 1–40, https://doi.org/10.5194/acp-2017-226, 2017.

Delanoë, J. and Hogan, R. J.: A variational scheme for retrieving ice cloud properties from combined radar, lidar, and infrared radiometer, J. Geophys. Res. Atmos., 113, https://doi.org/10.1029/2007JD009000, 2008.

Delanoë, J. and Hogan, R. J.: Combined CloudSat-CALIPSO-MODIS retrievals of the properties of ice clouds, J. Geophys. Res. Atmos., 115, https://doi.org/10.1029/2009JD012346, 2010.

5 Delanoë, J., Protat, A., Testud, J., Bouniol, D., Heymsfield, A. J., Bansemer, A., Brown, P. R. A., and Forbes, R. M.: Statistical properties of the normalized ice particle size distribution, J. Geophys. Res. Atmos., 110, https://doi.org/10.1029/2004JD005405, 2005.

Delanoë, J., Heymsfield, A. J., Protat, A., Bansemer, A., and Hogan, R. J.: Normalized particle size distribution for remote sensing application, J. Geophys. Res, 119, 4204–4227, https://doi.org/10.1002/2013JD020700, http://dx.doi.org/10.1002/2013JD020700, 2014.

Deng, M., Mace, G. G., Wang, Z., and Okamoto, H.: Tropical Composition, Cloud and Climate Coupling Experiment validation
10 for cirrus cloud profiling retrieval using CloudSat radar and CALIPSO lidar, Journal of Geophysical Research: Atmospheres, 115, https://doi.org/10.1029/2009JD013104, 2010.

Deng, M., Mace, G. G., Wang, Z., and Lawson, R. P.: Evaluation of Several A-Train Ice Cloud Retrieval Products with In Situ Measurements Collected during the SPARTICUS Campaign, J. Appl. Meteor. and Clim., 52, 1014–1030, https://doi.org/10.1175/JAMC-D-12-054.1, 2012.

15 Eliasson, S., Buehler, S. A., Milz, M., Eriksson, P., and John, V. O.: Assessing observed and modelled spatial distributions of ice water path using satellite data, Atmos. Chem. Phys., 11, 375–391, https://doi.org/10.5194/acp-11-375-2011, 2011.

Erfani, E. and Mitchell, D. L.: Developing and bounding ice particle mass- and area-dimension expressions for use in atmospheric models and remote sensing, Atmos. Chem. Phys., 16, 4379–4400, https://doi.org/10.5194/acp-16-4379-2016, 2016.

Farrington, R. J., Connolly, P. J., Lloyd, G., Bower, K. N., Flynn, M. J., Gallagher, M. W., Field, P. R., Dearden, C., and Choularton, T. W.:
20 Comparing model and measured ice crystal concentrations in orographic clouds during the INUPIAQ campaign, Atmos. Chem. Phys., 16, 4945–4966, https://doi.org/10.5194/acp-16-4945-2016, 2016.

Feofilov, A. G., Stubenrauch, C. J., and Delanoë, J.: Ice water content vertical profiles of high-level clouds: classification and impact on radiative fluxes, Atmos. Chem. Phys., 15, 12 327–12 344, https://doi.org/10.5194/acpd-15-16325-2015, 2015.

Field, P. R., Wood, R., Brown, P. R. A., Kaye, P. H., Hirst, E., Greenaway, R., and Smith, J. A.: Ice Particle Interarrival Times Measured with
25 a Fast FSSP, J. Atmos. Oceanic Technol., 20, 249–261, https://doi.org/10.1175/1520-0426(2003)020<0249:IPITMW>2.0.CO;2, 2003.

Field, P. R., Hogan, R. J., Brown, P. R. A., Illingworth, A. J., Choularton, T. W., and Cotton, R. J.: Parametrization of ice-particle size distributions for mid-latitude stratiform cloud, Quart. J. Roy. Meteor. Soc., 131, 1997–2017, https://doi.org/10.1256/qj.04.134, 2005.

Field, P. R., Heymsfield, A. J., and Bansemer, A.: Shattering and Particle Interarrival Times Measured by Optical Array Probes in Ice Clouds, J. Atmos. Oceanic Technol., 23, 1357–1371, https://doi.org/10.1175/JTECH1922.1, 2006.

30 Gasparini, B. and Lohmann, U.: Why cirrus cloud seeding cannot substantially cool the planet, J. Geophys. Res. Atmos., 121, 4877–4893, https://doi.org/10.1002/2015JD024666, 2016.

Gong, J. and Wu, D. L.: CloudSat-constrained cloud ice water path and cloud top height retrievals from MHS 157 and 183.3 GHz radiances, Atmos. Meas. Tech., 7, 1873–1890, https://doi.org/10.5194/amt-7-1873-2014, 2014.

Grosvenor, D. P., Sourdeval, O., Zuidema, P., Ackerman, A. S., Alexandrov, M. D., Bennartz, R., Boers, R., Cairns, B., Chiu, C., Christensen,
35 M., Deneke, H., Diamond, M., Feingold, G., Fridlind, A., Hünerbein, A., Knist, C., Kollias, P., Marshak, A., McCoy, D., Merk, D., Painemal, D., Rausch, J., Rosenfeld, D., Russchenberg, H., Seifert, P., Sinclair, K., Stier, P., van Diedenhoven, B., Wendisch, M., Werner, F., Wood, R., Zhang, Z., and Quaas, J.: Remote sensing of cloud droplet number concentration in warm clouds: Review of current state of knowledge and perspectives, Rev. Geophys., [in rev.], 2018.

Gryspeerdt, E., Quaas, J., and Bellouin, N.: Constraining the aerosol influence on cloud fraction, J. Geophys. Res. Atmos., 121, 3566–3583, https://doi.org/10.1002/2015JD023744, http://dx.doi.org/10.1002/2015JD023744, 2016.

Gryspeerdt, E., Quaas, J., Goren, T., Klocke, D., and Brueck, M.: Technical note: An automated cirrus classification, Atmos. Chem. Phys. Discuss., 2017, 1–18, https://doi.org/10.5194/acp-2017-723, 2017.

Gryspeerdt, E., Sourdeval, O., Quaas, J., Delanoë, J., and Kühne, P.: Ice crystal number concentration estimates from lidar-radar satellite retrievals. Part 2: Controls on the ice crystal number concentration, Atmos. Chem. Phys., [submitted], 2018.

Hendricks, J., Kärcher, B., and Lohmann, U.: Effects of ice nuclei on cirrus clouds in a global climate model, J. Geophys. Res. Atmos., 116, https://doi.org/10.1029/2010JD015302, 2011.

Heyn, I., Block, K., Mülmenstädt, J., Gryspeerdt, E., Kühne, P., Salzmann, M., and Quaas, J.: Assessment of simulated aerosol effective radiative forcings in the terrestrial spectrum, Geophys. Res. Lett., 44, 1001–1007, https://doi.org/10.1002/2016GL071975, 2017.

Holl, G., Eliasson, S., Mendrok, J., and Buehler, S. A.: SPARE-ICE: Synergistic ice water path from passive operational sensors, J. Geophys. Res. Atmos., 119, 1504–1523, https://doi.org/10.1002/2013JD020759, 2014.

Ickes, L., Welti, A., Hoose, C., and Lohmann, U.: Classical nucleation theory of homogeneous freezing of water: thermodynamic and kinetic parameters, Atmos. Chem. Phys., 17, 5514–5537, https://doi.org/10.1039/C4CP04184D, 2015.

Inoue, T.: On the temperature and effective emissivity determination of semi-transparent cirrus clouds by bi-spectral measurements in the 10 μm window region, J. Meteor. Soc. Japan, 63, 88–98, https://doi.org/10.2151/jmsj1965.63.1_88, 1985.

Jackson, R. C., McFarquhar, G. M., Fridlind, A. M., and Atlas, R.: The dependence of cirrus gamma size distributions expressed as volumes in N0-λ-μ phase space and bulk cloud properties on environmental conditions: Results from the Small Ice Particles in Cirrus Experiment (SPARTICUS), Journal of Geophysical Research: Atmospheres, 120, 10,351–10,377, https://doi.org/10.1002/2015JD023492, 2015.

Jensen, E. J., Toon, O. B., Westphal, D. L., Kinne, S., and Heymsfield, A. J.: Microphysical modeling of cirrus: 1. Comparison with 1986 FIRE IFO measurements, J. Geophys. Res. Atmos., 99, 10 421–10 442, https://doi.org/10.1029/93JD02334, 1994.

Jensen, E. J., Pfister, L., Jordan, D. E., Bui, T. V., Ueyama, R., Singh, H. B., Thornberry, T., Rollins, A. W., Gao, R.-S., Fahey, D. W., Rosenlof, K. H., Elkins, J. W., Diskin, G. S., DiGangi, J. P., Lawson, R. P., Woods, S., Atlas, E. L., Navarro Rodriguez, M. A., Wofsy, S. C., Pittman, J., Bardeen, C. G., Toon, O. B., Kindel, B. C., Newman, P. A., McGill, M. J., Hlavka, D. L., Lait, L. R., Schoeberl, M. R., Bergman, J. W., Selkirk, H. B., Alexander, M. J., Kim, J.-E., Lim, B. H., Stutz, J., and Pfeilsticker, K.: The NASA Airborne Tropical TRopopause EXperiment (ATTREX): High-Altitude Aircraft Measurements in the Tropical Western Pacific, Bull. Amer. Meteor. Soc., 98, 129–143, https://doi.org/10.1175/BAMS-D-14-00263.1, 2015.

Kärcher, B. and Lohmann, U.: A parameterization of cirrus cloud formation: Homogeneous freezing of supercooled aerosols, J. Geophys. Res. Atmos., 107, https://doi.org/10.1029/2001JD000470, 2002.

Kärcher, B. and Lohmann, U.: A parameterization of cirrus cloud formation: Heterogeneous freezing, J. Geophys. Res. Atmos., 108, https://doi.org/10.1029/2002JD003220, 2003.

Kärcher, B. and Ström, J.: The roles of dynamical variability and aerosols in cirrus cloud formation, Atmos. Chem. Phys., 3, 823–838, https://doi.org/10.5194/acp-3-823-2003, 2003.

Kay, J. E. and Wood, R.: Timescale analysis of aerosol sensitivity during homogeneous freezing and implications for upper tropospheric water vapor budgets, Geophys. Res. Lett., 35, https://doi.org/10.1029/2007GL032628, 2008.

Khain, A., Ovtchinnikov, M., Pinsky, M., Pokrovsky, A., and Krugliak, H.: Notes on the state-of-the-art numerical modeling of cloud microphysics, Atmos. Res., 55, 159 – 224, https://doi.org/10.1016/S0169-8095(00)00064-8, 2000.

King, M. D., Tsay, S. C., Platnick, S., Wang, M., and Liou, K. N.: Cloud Retrieval Algorithms for MODIS: Optical Thickness, Effective Particle Radius, and Thermodynamic Phase., Algorithm Theor. Basis Doc. ATBD-MOD-05, NASA Goddard Space Flight Cent., Greenbelt, Md., 1998.

Koop, T., Luo, B., Tsias, A., and Peter, T.: Water activity as the determinant for homogeneous ice nucleation in aqueous solutions, Nature, 406, 611–614, https://doi.org/10.1038/35020537, 2000.

Korolev, A. and Field, P. R.: Assessment of the performance of the inter-arrival time algorithm to identify ice shattering artifacts in cloud particle probe measurements, Atmos. Meas. Tech., 8, 761–777, https://doi.org/10.5194/amt-8-761-2015, 2015.

Korolev, A., Emery, E. F., Strapp, J. W., Cober, S. G., Isaac, G. A., Wasey, M., and Marcotte, D.: Small Ice Particles in Tropospheric Clouds: Fact or Artifact? Airborne Icing Instrumentation Evaluation Experiment, Bull. Amer. Meteorol. Soc., 92, 967–973, https://doi.org/10.1175/2010BAMS3141.1, 2011.

Korolev, A. V., Emery, E. F., Strapp, J. W., Cober, S. G., and Isaac, G. A.: Quantification of the Effects of Shattering on Airborne Ice Particle Measurements, Journal of Atmospheric and Oceanic Technology, 30, 2527–2553, https://doi.org/10.1175/JTECH-D-13-00115.1, https://doi.org/10.1175/JTECH-D-13-00115.1, 2013.

Krämer, M., Rolf, C., Luebke, A., Afchine, A., Spelten, N., Costa, A., Meyer, J., Zöger, M., Smith, J., Herman, R. L., Buchholz, B., Ebert, V., Baumgardner, D., Borrmann, S., Klingebiel, M., and Avallone, L.: A microphysics guide to cirrus clouds – Part 1: Cirrus types, Atmos. Chem. Phys., 16, 3463–3483, https://doi.org/10.5194/acp-16-3463-2016, 2016.

Lawson, R. P.: Effects of ice particles shattering on the 2D-S probe, Atmos. Meas. Tech., 4, 1361–1381, https://doi.org/10.5194/amt-4-1361-2011, http://www.atmos-meas-tech.net/4/1361/2011/, 2011.

Lawson, R. P., O'Connor, D., Zmarzly, P., Weaver, K., Baker, B., Mo, Q., and Jonsson, H.: The 2D-S (Stereo) Probe: Design and Preliminary Tests of a New Airborne, High-Speed, High-Resolution Particle Imaging Probe, J. Atmos. Oceanic Technol., 23, 1462–1477, https://doi.org/10.1175/JTECH1927.1, 2006.

Liou, K.: Influence of cirrus clouds on weather and climate processes: A global perspective, Mon. Wea. Rev., 114, 1167–1199, https://doi.org/10.1175/1520-0493(1986)114<1167:IOCCOW>2.0.CO;2, 1986.

Lohmann, U., Quaas, J., Kinne, S., and Feichter, J.: Different Approaches for Constraining Global Climate Models of the Anthropogenic Indirect Aerosol Effect, Bull. Amer. Meteor. Soc, 88, 243–249, https://doi.org/10.1175/BAMS-88-2-243, 2007.

Luebke, A. E., Afchine, A., Costa, A., Grooß, J.-U., Meyer, J., Rolf, C., Spelten, N., Avallone, L. M., Baumgardner, D., and Krämer, M.: The origin of midlatitude ice clouds and the resulting influence on their microphysical properties, Atmos. Chem. Phys., 16, 5793–5809, https://doi.org/10.5194/acp-16-5793-2016, 2016.

Mace, J., Jensen, E., McFarquhar, G., Comstock, J., Ackerman, T., Mitchell, D., Liu, X., and Garrett, T.: SPartICus: Small Particles In Cirrus science and operations plan, Tech. rep., ARM, Available at https://www.arm.gov/publications/programdocs/doe-sc-arm-10-003.pdf, 2009.

Massie, S. T., Delanoë, J., Bardeen, C. G., Jiang, J. H., and Huang, L.: Changes in the shape of cloud ice water content vertical structure due to aerosol variations, Atmos. Chem. Phys., 16, 6091–6105, https://doi.org/10.5194/acp-16-6091-2016, 2016.

McFarquhar, G. M., Um, J., Freer, M., Baumgardner, D., Kok, G. L., and Mace, G.: Importance of small ice crystals to cirrus properties: Observations from the Tropical Warm Pool International Cloud Experiment (TWP-ICE), Geophysical Research Letters, 34, https://doi.org/10.1029/2007GL029865, 2007.

Mesinger, F., DiMego, G., Kalnay, E., Mitchell, K., Shafran, P. C., Ebisuzaki, W., Jović, D., Woollen, J., Rogers, E., Berbery, E. H., Ek, M. B., Fan, Y., Grumbine, R., Higgins, W., Li, H., Lin, Y., Manikin, G., Parrish, D., and Shi, W.: North American Regional Reanalysis, Bull. Amer. Meteor. Soc., 87, 343–360, https://doi.org/10.1175/BAMS-87-3-343, 2006.

Meyer, J.: Ice Crystal Measurements with the New Particle Spec- trometer NIXE-CAPS, Ph.D. thesis, Schriften des Forschungszentrum Jülich, Reihe Energie und Umwelt, 2012.

Mishra, S., Mitchell, D. L., Turner, D. D., and Lawson, R. P.: Parameterization of ice fall speeds in midlatitude cirrus: Results from SPartICus, J. Geophys. Res. Atmos., 119, 3857–3876, https://doi.org/10.1002/2013JD020602, 2014.

5   Mitchell, D., Mishra, S., and Lawson, P.: Cirrus Clouds and Climate Engineering: New Findings on Ice Nucleation and Theoretical Basis, in: Planet Earth 2011 - Global Warming Challenges and Opportunities for Policy and Practice, edited by Carayannis, E., InTech, https://doi.org/10.5772/24664, 2011.

Mitchell, D. L.: Use of Mass- and Area-Dimensional Power Laws for Determining Precipitation Particle Terminal Velocities, J. Atmos. Sci., 53, 1710–1723, https://doi.org/10.1175/1520-0469(1996)053<1710:UOMAAD>2.0.CO;2, 1996.

10   Mitchell, D. L., d'Entremont, R. P., and Lawson, R. P.: Inferring Cirrus Size Distributions through Satellite Remote Sensing and Microphysical Databases, J. Atmos. Sci., 67, 1106–1125, https://doi.org/10.1175/2009JAS3150.1, 2010.

Mitchell, D. L., Garnier, A., Avery, M., and Erfani, E.: CALIPSO observations of the dependence of homo- and heterogeneous ice nucleation in cirrus clouds on latitude, season and surface condition, Atmos. Chem. Phys. Discuss., 2016, 1–60, https://doi.org/10.5194/acp-2016-1062, 2016.

15   Nakajima, T. and King, M. D.: Determination of the Optical Thickness and Effective Particle Radius of Clouds from Reflected Solar Radiation Measurements. Part I: Theory, J. Atmos. Sci., 47, 1878–1893, https://doi.org/10.1175/1520-0469, 1990.

Noel, V., Hertzog, A., Chepfer, H., and Winker, D. M.: Polar stratospheric clouds over Antarctica from the CALIPSO spaceborne lidar, J. Geophys. Res. Atmos., 113, https://doi.org/10.1029/2007JD008616, 2008.

Osborne, S. R., Abel, S. J., Boutle, I. A., and Marenco, F.: Evolution of Stratocumulus Over Land: Comparison of Ground and Aircraft Observations with Numerical Weather Prediction Simulations, Boundary-Layer Meteorology, 153, 165–193, https://doi.org/10.1007/s10546-014-9944-0, 2014.

Painemal, D. and Zuidema, P.: Assessment of MODIS cloud effective radius and optical thickness retrievals over the Southeast Pacific with VOCALS-REX in situ measurements, J. Geophys. Res. Atmos., 116, https://doi.org/10.1029/2011JD016155, 2011.

Protat, A., Delanoë, J., O'Connor, E. J., and L'Ecuyer, T. S.: The Evaluation of CloudSat and CALIPSO Ice Microphysical Products Using Ground-Based Cloud Radar and Lidar Observations, J. Atmos. Oceanic Technol., 27, 793–810, https://doi.org/10.1175/2009JTECHA1397.1, 2010.

Protat, A., Young, S. A., McFarlane, S. A., L'Ecuyer, T., Mace, G. G., Comstock, J. M., Long, C. N., Berry, E., and Delanoë, J.: Reconciling Ground-Based and Space-Based Estimates of the Frequency of Occurrence and Radiative Effect of Clouds around Darwin, Australia, J. Appl. Meteor. and Clim., 53, 456–478, https://doi.org/10.1175/JAMC-D-13-072.1, 2014.

30   Quaas, J., Boucher, O., and Lohmann, U.: Constraining the total aerosol indirect effect in the LMDZ and ECHAM4 GCMs using MODIS satellite data, Atmos. Chem. Phys., 6, 947–955, https://doi.org/10.5194/acp-6-947-2006, 2006.

Quaas, J., Boucher, O., Bellouin, N., and Kinne, S.: Satellite-based estimate of the direct and indirect aerosol climate forcing, J. Geophys. Res. Atmos., 113, https://doi.org/10.1029/2007JD008962, 2008.

Schmid, B., Tomlinson, J. M., Hubbe, J. M., Comstock, J. M., Mei, F., Chand, D., Pekour, M. S., Kluzek, C. D., Andrews, E., Biraud, S. C.,

35   and McFarquhar, G. M.: The DOE ARM Aerial Facility, Bull. Amer. Meteor. Soc., 95, 723–742, https://doi.org/10.1175/BAMS-D-13-00040.1, 2013.

Seifert, A. and Beheng, K. D.: A two-moment cloud microphysics parameterization for mixed-phase clouds. Part 1: Model description, Meteor. Atmos. Phys., 92, 45–66, https://doi.org/10.1007/s00703-005-0112-4, 2006.

Sourdeval, O., Labonnote, L. C., Brogniez, G., Jourdan, O., Pelon, J., and Garnier, A.: A variational approach for retrieving ice cloud properties from infrared measurements: application in the context of two IIR validation campaigns, Atmos. Chem. Phys., 13, 8229–8244, https://doi.org/10.5194/acp-13-8229-2013, http://www.atmos-chem-phys.net/13/8229/2013/, 2013.

Sourdeval, O., C. Labonnote, L., Baran, A. J., and Brogniez, G.: A methodology for simultaneous retrieval of ice and liquid water cloud properties. Part I: Information content and case study, Quart. J. Roy. Meteor. Soc., 141, 870–882, https://doi.org/10.1002/qj.2405, 2015.

Sourdeval, O., C. Labonnote, L., Baran, A. J., Mülmenstädt, J., and Brogniez, G.: A methodology for simultaneous retrieval of ice and liquid water cloud properties. Part 2: Near-global retrievals and evaluation against A-Train products, Quart. J. Roy. Meteor. Soc., 142, 3063–3081, https://doi.org/10.1002/qj.2889, 2016.

Stein, A. F., Draxler, R. R., Rolph, G. D., Stunder, B. J. B., Cohen, M. D., and Ngan, F.: NOAA's HYSPLIT Atmospheric Transport and Dispersion Modeling System, Bull. Amer. Meteor. Soc., 96, 2059–2077, https://doi.org/10.1175/BAMS-D-14-00110.1, 2015.

Stephens, G. L.: Cloud Feedbacks in the Climate System: A Critical Review, J. Clim., 18, 237–273, https://doi.org/10.1175/JCLI-3243.1, 2005.

Stephens, G. L., Tsay, S.-C., Stackhouse, P. W., and Flatau, P. J.: The Relevance of the Microphysical and Radiative Properties of Cirrus Clouds to Climate and Climatic Feedback, Journal of the Atmospheric Sciences, 47, 1742–1754, 1990.

Stephens, G. L., Vane, D. G., Boain, R. J., Mace, G. G., Sassen, K., Wang, Z., Illingworth, A. J., O'Connor, E. J., Rossow, W. B., Durden, S. L., Miller, S. D., Austin, R. T., Benedetti, A., Mitrescu, C., and CloudSat Science Team, T.: The CLOUDSAT Mission and the A-Train, Bull. Amer. Meteor. Soc., 83, 1771–1790, https://doi.org/10.1175/BAMS-83-12-1771, 2002.

Thornberry, T. D., Rollins, A. W., Avery, M. A., Woods, S., Lawson, R. P., Bui, T. V., and Gao, R.-S.: Ice water content-extinction relationships and effective diameter for TTL cirrus derived from in situ measurements during ATTREX 2014, J. Geophys. Res. Atmos., 122, 4494–4507, https://doi.org/10.1002/2016JD025948, 2017.

Vaughan, M., Powell, K., Kuehn, R., Young, S., Winker, D., Hostetler, C., Hunt, W., Liu, Z., McGill, M., and Getzewich, B.: Fully Automated Detection of Cloud and Aerosol Layers in the CALIPSO Lidar Measurements, J. Atmos. Oceanic Technol., 26, 2034–2050, https://doi.org/10.1175/2009JTECHA1228.1, 2009.

Voigt, C., Schumann, U., Minikin, A., Abdelmonem, A., Afchine, A., Borrmann, S., Boettcher, M., Buchholz, B., Bugliaro, L., Costa, A., Curtius, J., Dollner, M., Dörnbrack, A., Dreiling, V., Ebert, V., Ehrlich, A., Fix, A., Forster, L., Frank, F., Fütterer, D., Giez, A., Graf, K., Grooß, J.-U., Groß, S., Heimerl, K., Heinold, B., Hüneke, T., Järvinen, E., Jurkat, T., Kaufmann, S., Kenntner, M., Klingebiel, M., Klimach, T., Kohl, R., Krämer, M., Krisna, T. C., Luebke, A., Mayer, B., Mertes, S., Molleker, S., Petzold, A., Pfeilsticker, K., Port, M., Rapp, M., Reutter, P., Rolf, C., Rose, D., Sauer, D., Schäfler, A., Schlage, R., Schnaiter, M., Schneider, J., Spelten, N., Spichtinger, P., Stock, P., Walser, A., Weigel, R., Weinzierl, B., Wendisch, M., Werner, F., Wernli, H., Wirth, M., Zahn, A., Ziereis, H., and Zöger, M.: ML-CIRRUS: The Airborne Experiment on Natural Cirrus and Contrail Cirrus with the High-Altitude Long-Range Research Aircraft HALO, Bull. Amer. Meteor. Soc., 98, 271–288, https://doi.org/10.1175/BAMS-D-15-00213.1, 2016.

Waliser, D. E., Li, J.-L. F., Woods, C. P., Austin, R. T., Bacmeister, J., Chern, J., Del Genio, A., Jiang, J. H., Kuang, Z., Meng, H., Minnis, P., Platnick, S., Rossow, W. B., Stephens, G. L., Sun-Mack, S., Tao, W.-K., Tompkins, A. M., Vane, D. G., Walker, C., and Wu, D.: Cloud ice: A climate model challenge with signs and expectations of progress, J. Geophys. Res., 114, https://doi.org/10.1029/2008JD010015, 2009.

Wendisch, M., Pöschl, U., Andreae, M. O., Machado, L. A. T., Albrecht, R., Schlager, H., Rosenfeld, D., Martin, S. T., Abdelmonem, A., Afchine, A., Araùjo, A. C., Artaxo, P., Aufmhoff, H., Barbosa, H. M. J., Borrmann, S., Braga, R., Buchholz, B., Cecchini, M. A., Costa, A., Curtius, J., Dollner, M., Dorf, M., Dreiling, V., Ebert, V., Ehrlich, A., Ewald, F., Fisch, G., Fix, A., Frank, F., Fütterer, D., Heckl, C., Heidelberg, F., Hüneke, T., Jäkel, E., Järvinen, E., Jurkat, T., Kanter, S., Kästner, U., Kenntner, M., Kesselmeier, J., Klimach, T., Knecht,

M., Kohl, R., Kölling, T., Krämer, M., Krüger, M., Krisna, T. C., Lavric, J. V., Longo, K., Mahnke, C., Manzi, A. O., Mayer, B., Mertes, S., Minikin, A., Molleker, S., Münch, S., Nillius, B., Pfeilsticker, K., Pöhlker, C., Roiger, A., Rose, D., Rosenow, D., Sauer, D., Schnaiter, M., Schneider, J., Schulz, C., de Souza, R. A. F., Spanu, A., Stock, P., Vila, D., Voigt, C., Walser, A., Walter, D., Weigel, R., Weinzierl, B., Werner, F., Yamasoe, M. A., Ziereis, H., Zinner, T., and Zöger, M.: ACRIDICON–CHUVA Campaign: Studying Tropical Deep Convective Clouds and Precipitation over Amazonia Using the New German Research Aircraft HALO, Bull. Amer. Meteor. Soc., 97, 1885–1908, https://doi.org/10.1175/BAMS-D-14-00255.1, 2016.

Wu, D. L., Austin, R. T., Deng, M., Durden, S. L., Heymsfield, A. J., Jiang, J. H., Lambert, A., Li, J.-L., Livesey, N. J., McFarquhar, G. M., Pittman, J. V., Stephens, G. L., Tanelli, S., Vane, D. G., and Waliser, D. E.: Comparisons of global cloud ice from MLS, CloudSat, and correlative data sets, J. Geophys. Res. Atmos., 114, https://doi.org/10.1029/2008JD009946, 2009.

Zhang, K., Liu, X., Wang, M., Comstock, J. M., Mitchell, D. L., Mishra, S., and Mace, G. G.: Evaluating and constraining ice cloud parameterizations in CAM5 using aircraft measurements from the SPARTICUS campaign, Atmos. Chem. Phys., 13, 4963–4982, https://doi.org/10.5194/acp-13-4963-2013, 2013.

Zhang, Y., Macke, A., and Albers, F.: Effect of crystal size spectrum and crystal shape on stratiform cirrus radiative forcing, Atmos. Res., 52, 59–75, 1999.